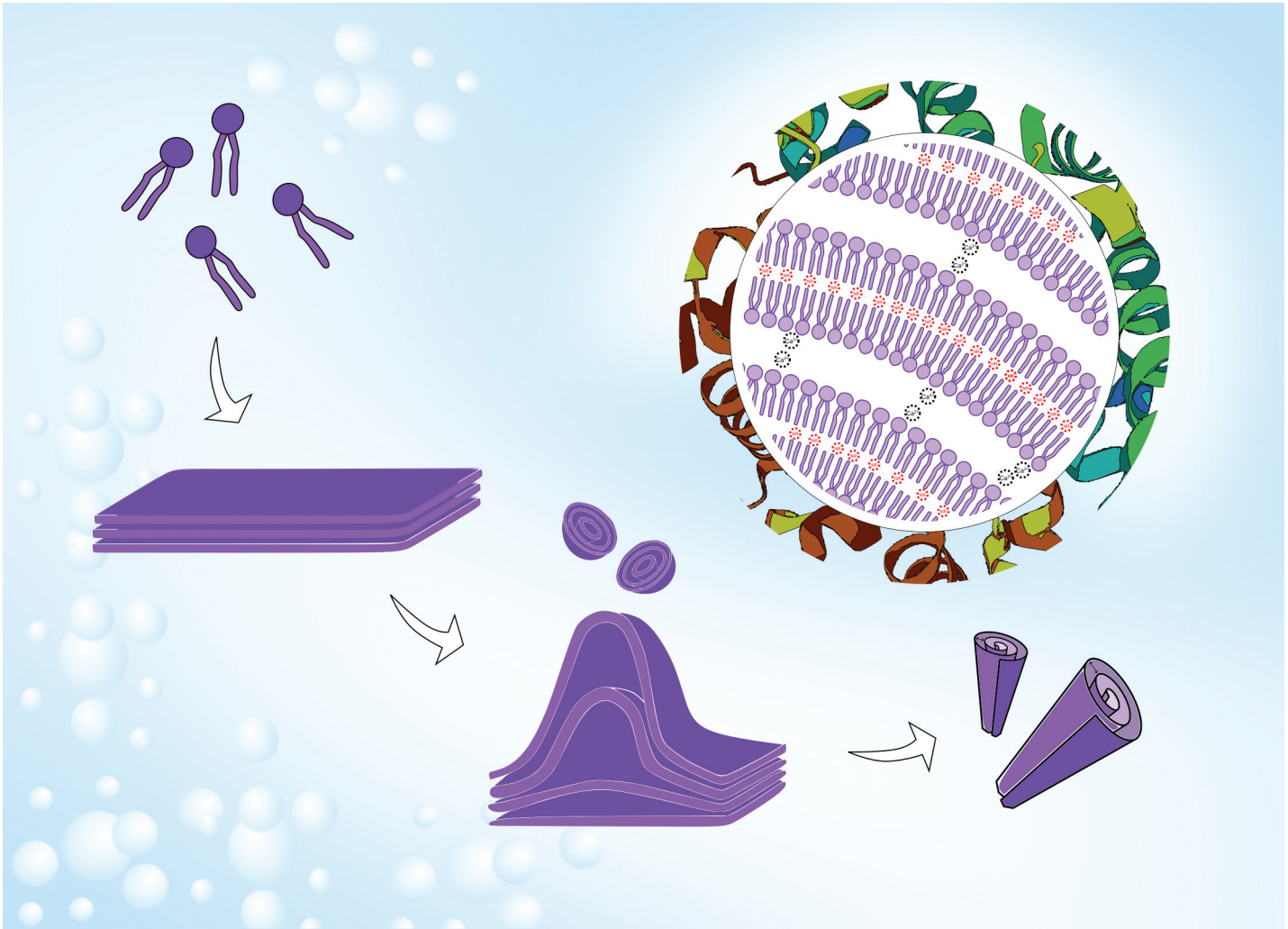

Showcasing collaborative research from Dr Rahul Shukla Department of Pharmaceutics, National Institute of Pharmaceutical Education and Research (NIPER- R), Raebareli, India and Professor Kamalinder K Singh, School of Pharmacy and Biomedical Sciences, University of Lancashire, Preston, United Kingdom.

Naringenin-encapsulated nano-cochleate hydrogel for topical delivery: cellular anti-inflammatory activity and dermatokinetic profiling

Encapsulating naringenin — a poorly water soluble, plant derived flavonoid — into nano cochleates embedded within a hydrogel matrix significantly enhances its physicochemical and biological performance. This delivery system improves naringenin's aqueous dispersibility, cellular uptake, and anti-inflammatory activity, while demonstrating strong ROS scavenging capacity. In addition, the hydrogel based nano cochleates promote superior skin permeation and retention, indicating strong potential for the topical management of psoriasis.

Image reproduced by permission of Ashish Dilip Sutar, Kamalinder K Singh, Rahul Shukla from *RSC Pharm.*, 2026, **3**, 401-422

As featured in:

See Kamalinder K. Singh, Rahul Shukla *et al., RSC Pharm.*, 2026, **3**, 401.

ROYAL SOCIETY OF CHEMISTRY

rsc.li/RSCPharma

Registered charity number: 207890

RSC Pharmaceutics

ROYAL SOCIETY OF CHEMISTRY

PAPER

View Article Online
View Journal | View Issue

Cite this: *RSC Pharm.*, 2026, **3**, 401

Naringenin-encapsulated nano-cochleate hydrogel for topical delivery: cellular anti-inflammatory activity and dermatokinetic profiling

Anuja Shashikant Kamble,†[a] Ashish Dilip Sutar,†[a] Gagandeep Kaur,[a] Kamalinder K. Singh *[b,c] and Rahul Shukla*[a]

Naringenin (NR) is a plant-based flavonoid with poor aqueous solubility, which is indicated for the treatment of psoriasis due to its strong antioxidant and anti-inflammatory properties. The aim of this study was to evaluate the non-steroidal NR-loaded nanocochleate hydrogel (NR-NC-G) for its skin permeation, safety, and efficacy in the treatment of psoriasis. First, nanoliposomes (NR-LIPO) were prepared and further chelated using calcium chloride to transform them into nanocochleates (NR-NCs). NR-NCs exhibited rolled sheet-like nanosized particles with a hydrodynamic diameter of approximately 160–170 nm, an encapsulation efficiency of 81–82%, and good colloidal stability, as indicated by a ζ-potential of −27 mV. To achieve a local reservoir-like action, nanocochleates were loaded into a hydrogel comprising of combination of Carbopol 934P and sodium alginate. NR-NC-G was characterised for its physical and rheological characteristics, and it exhibited uniform drug loading, long-term stability, and the ability to scavenge reactive oxygen species (ROS), as validated by various antioxidant assays. Furthermore, NR-NC-G reduced cellular ROS levels, nitrate accumulation, and mitochondrial healing ability in a lipopolysaccharide-stimulated RAW264.7 inflammation model, thereby proving its enhanced antioxidant and anti-inflammatory effects. The *ex vivo* skin permeation and dermatokinetic studies showed that NR-NC-G exhibited high permeation across the excised skin of BALB/C mice. The dermatokinetic studies showed that topical application of NR-NC-G provided 3.43 and 3.34-fold greater C_{max} and AUC_{0-t} in the epidermal layer, respectively, compared to the bulk NR solution. Overall, this novel nanoformulation enhances ROS scavenging capacity, improves cellular uptake, enhances skin permeation and retention, and suggests potential applications for treating psoriasis.

Received 30th September 2025,
Accepted 16th December 2025

DOI: 10.1039/d5pm00268k

rsc.li/RSCPharma

1. Introduction

Psoriasis is a chronic autoimmune skin disease marked by fast keratinocyte proliferation, epidermal hyperplasia, and inflammatory infiltration.[1] Its pathogenesis involves overexpression of inflammatory mediators like TNF-α, IL-6, and IL-17, along with increased oxidative stress (Fig. 1a).[2–4] Traditional topical treatments, such as corticosteroids and calcineurin inhibitors, generally lead to local irritation, and drugs like methotrexate carry risks of immunosuppression and hepatotoxicity.[5,6]

Naringenin (NR), a plant-based citrus flavonoid, has dual antioxidant and anti-inflammatory properties by modulating NF-κB and Nrf2 (Fig. 1e) pathways according to various reported studies.[7] Because of its anti-inflammatory activity and inhibitory activity on chemokine production, reports have demonstrated its potential use in psoriasis.[8,9] But its therapeutic efficacy is compromised by poor aqueous solubility, chemical instability, and limited bioavailability (~5–9%) because of high first-pass metabolism and low permeability.[7,10,11]

To overcome these limitations, nanocarrier systems have been investigated.[11] While traditional nanoparticulate systems enhance solubility, their colloidal instability and low dermal retention limit their clinical effectiveness.[12] Nanocochleates (NCs) are sustained-release depot systems composed of phos-

[a]*Department of Pharmaceutics, National Institute of Pharmaceutical Education and Research (NIPER-Raebareli), Bijnor-Sisendi Road, Sarojini Nagar, Near CRPF Base Camp, Lucknow, UP, 226002, India. E-mail: rahulshuklapharm@gmail.com, rahul.shukla@niperraebareli.edu.in*
[b]*School of Pharmacy and Biomedical Sciences, University of Lancashire, Preston PR1 2HE, UK. E-mail: KSingh1@lancashire.ac.uk*
[c]*Biomedical Evidence based Transdisciplinary (BEST) Health Research Institute, University of Lancashire, Preston PR1 2HE, UK*
†Authors contributed equally.

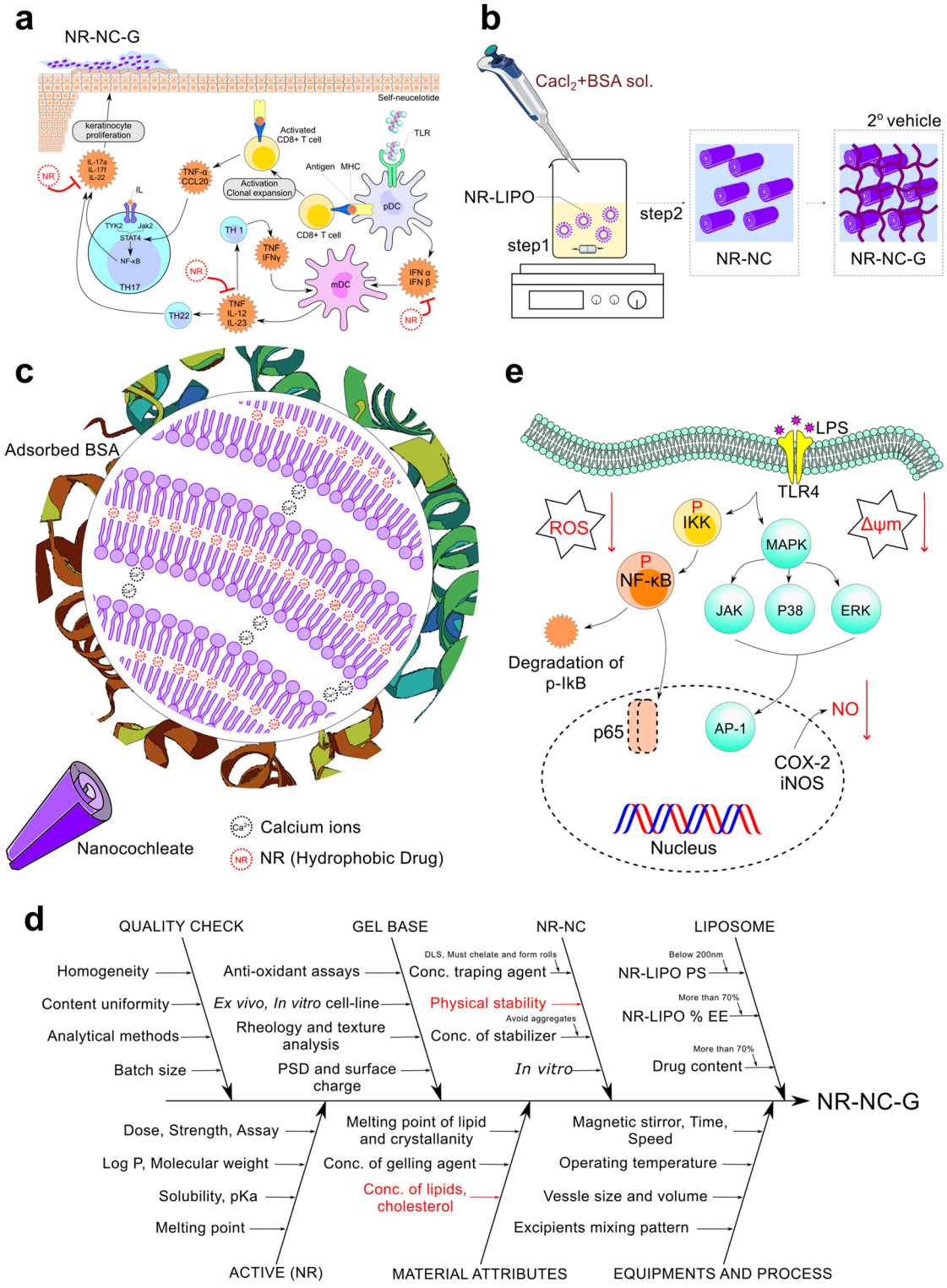

Fig. 1 Schematic presentation of (a) the proposed pathway of psoriasis treatment upon the application of topical NR-NC-G (the hydrogel penetrates deeply into the dermal layers, it suppresses the immunoinflammatory response of cytokines, which leads to the alleviation of psoriasis); (b) method of preparation for NR-NC-G; (c) internal structure of NR-NCs; (d) Ishikawa fishbone diagram for evaluating the quality targeted product profile; and (e) cellular molecular mechanism showing the anti-inflammatory and antioxidant activities of NR-NC-G *in vitro*. The formulation modulates key signalling pathways, including NF-κB, MAPK, and Nrf2/HO-1.

pholipid precipitates that self-assemble from anionic lipid vesicles binding to divalent cations, such as Ca^{2+}. They consist of a uniform, solid-lipid bilayer sheet that is rolled in a supramolecular pattern (Fig. 1c).[12] Nanosize, industrial feasibility, cytocompatibility, fewer side effects, and higher effectiveness are a few of the advantages of NCs that allow them to be explored in topical drug delivery.

Recent advances in hydrogel engineering highlight their capacity to provide sustained, localised drug delivery while resisting mechanical stress in challenging biological environments.[13–15] Dual-network and stimuli-responsive hydrogels have demonstrated improved structural stability, controlled release, and enhanced therapeutic efficacy across various applications.[16–19] These systems underscore the broader potential of hydrogel platforms to optimise bioavailability, modulate local microenvironments, and support tissue repair.[20,21] Such progress provides a strong rationale for developing novel hydrogel-based carriers for topical anti-inflammatory therapeutics such as naringenin.

Embedding NCs into a Carbopol-based hydrogel further enhances topical application by improving spreadability, bioadhesion, and drug residence time at the site of application. In the present study, a naringenin nanocochleate-loaded hydrogel (NR-NC-G) was developed using a Quality by Design (QbD) approach and evaluated for its physicochemical, dermatokinetic, and biological performance to check its potential for topical treatment of psoriasis.

2. Materials and methods

2.1. Materials

Naringenin was purchased from Tokyo Chemical Industry Co., Ltd. Lipoid-S-100 was a gift from Lipoid GmbH, Germany, and cholesterol was procured from Hi-Media. Various excipients, including calcium chloride, Carbopol 934, triethanolamine, bovine serum albumin (BSA), and sodium alginate, were obtained from Sisco Research Laboratories. Dulbecco's modified Eagle's medium (DMEM), fetal bovine serum (FBS), 3-(4,5-dimethylthiazol-2-yl)-2,5-diphenyltetrazolium bromide (MTT), dichlorodihydrofluorescein diacetate (DCFDA), 5,5′,6,6′-tetrachloro-1,1′,3,3′-tetraethylbenzimidazolocarbocyanine iodide (JC-1), lipopolysaccharide (LPS), *etc*., were procured from Hi-Media. The organic solvents used are of HPLC grade, and the entire formulation procedure was carried out with triple-distilled Milli-Q water.

3. Methods

3.1. Drug quantification

NR was solubilised in methanol to make a stock solution and serially diluted to prepare working standards of 2, 4, 6, 8, and 10 μg mL^{-1} for λ_{max} determination and calibration curve construction using a UV-visible spectrophotometer (Cary 60, UV-Visible spectrophotometer, Agilent). Furthermore, an HPLC analytical method was developed and validated for the quantification of NR in skin samples. Chromatographic detection was performed using a C18 column (250 mm, 4.6 μm) under isocratic conditions with a mobile phase of 80% water and 20% methanol (v/v) at a flow rate of 1.2 mL min^{-1}. The detector was set at 288 nm. The injection volume was 10 μL, and the column temperature was maintained at 25 °C.[22,23]

3.2. Nanocochleate (NR-NC) formulation

A QbD approach was used to systematically develop NR-loaded liposomes (NR-LIPOs). This approach was followed in accordance with the ICH Q8 and Q9 guidelines, starting with the definition of the Quality Target Product Profile (QTPP) and the identification of Critical Quality Attributes (CQAs), Critical Material Attributes (CMAs), and Critical Process Parameters (CPPs).[24] Particle size (PS) and percent encapsulation efficiency (EE%) were defined as the main CQAs. An Ishikawa (fishbone) diagram (Fig. 1d) was constructed to identify factors affecting the quality and reproducibility of the NR-NC-G system. Key parameters included the properties of NR, lipid and gel material attributes, nanocochleate-formation parameters, and equipment conditions. Each sub-factor, such as the lipid/cholesterol ratio, calcium concentration, stabiliser level, rheology of the gel base, and mixing parameters, was mapped based on early experimental observations. This served as a structured framework to guide risk assessment, parameter control, and optimisation throughout formulation development.

In the first step, NR-LIPOs were formulated using the thin film hydration technique. Lipoid-S-100, cholesterol, and NR were dissolved in a sufficient quantity of chloroform, and the solvent was evaporated using a rotary evaporator to form a thin film, which was further hydrated with Milli-Q water to form liposomes. A custom experimental design was applied to optimise Lipoid-S-100 and cholesterol concentrations as independent variables, with the hydrodynamic diameter (HD) and percent encapsulation efficiency (%EE) as response variables.

In the second phase (Fig. 1b), NR-loaded nanocochleates (NR-NCs) were fabricated *via* the trapping method. Calcium chloride was added in varying volumes to the optimised liposomal suspension and vortexed for 2 minutes to induce structural reorganisation.[12,25] Dynamic light scattering (DLS) was employed to assess the changes, and the optimal volume was selected based on the resulting data. Bovine serum albumin (BSA) was incorporated as an aggregation inhibitor. The secondary structure of the developed NCs was evaluated using circular dichroism (CD) spectroscopy to detect any conformational changes in comparison with the BSA solution.

3.3. Characterisation of NR-NCs

3.3.1. Hydrodynamic diameter, homogeneity, and ζ-potential. The HD, ζ-potential, and polydispersity index (PDI) of NR-NCs were determined using DLS on a Malvern Zetasizer

(Nano ZS, Malvern, United Kingdom). The formulation was diluted 10 times for particle size measurement in a particle size-specific cuvette, and the zeta potential was checked for the undiluted sample.[26]

3.3.2. Percent encapsulation efficiency (%EE). The NR-NC dispersion was centrifuged at 10 000 rpm and 4 °C for 45 minutes to investigate the %EE. The supernatant was collected and analysed using UV-Visible spectrophotometry at an appropriate wavelength. The percentage EE was calculated using the formula given in eqn (1).[27]

$$\% \text{ EE} = [\text{conc. total} - \text{conc. free drug}] \div \text{conc. total} \times 100 \quad (1)$$

Conc. total = total initial drug concentration in mg and conc. free drug = free drug concentration in mg.

3.3.3. Surface morphological assessment. The surface morphology of NR-NCs was observed using scanning electron microscopy (SEM), transmission electron microscopy (TEM) and atomic force microscopy (AFM). For TEM (JEM-2100; JEOL Ltd, Tokyo, Japan), the NR-NCs were diluted, placed on a carbon-coated copper grid, dried, and then imaged. In SEM (JSM-IT200, JEOL, Japan), the diluted sample was placed on a stub using carbon tape, dried, and scanned to obtain images. In AFM (NX12, Park System, Korea), non-contact mode was employed, and the samples were diluted with Milli-Q water and then dried in a desiccator. Scanning was performed at 0.5 Hz.[27,28]

3.3.4. Thermal analysis. Bulk NR, the physical mixture, and lyophilised NR-NCs were analysed using differential scanning calorimeter (DSC) equipment (TA Instruments, New Castle, USA) in hermetically sealed aluminium pans. 2–3 mg of sample for analysis is sealed and heated at a gradual increase in temperature of 10 °C per minute in the range from 10 °C to 300 °C.[29–31]

3.3.5. Attenuated total reflectance infrared spectroscopy (ATR-IR). The ATR-IR spectrometer (Waltham, Massachusetts, U.S.), set between 4000 and 600 cm^{-1} wave numbers, was used to measure frequencies. To assess the compatibility of the drug and excipients, shifts in the peaks were analysed to evaluate the compatibility and possible molecular interactions.[32,33]

3.3.6. Powder X-ray diffraction study. For their crystal properties, the bulk NR and the lyophilised NR-NCs were examined using an X-ray diffractometer (XRD, Brucker AXS-D8 advance®, Karlsruhe, Germany). Diffractograms were recorded in a scanning range from 5° to 90° on a 2θ scale.[34]

3.3.7. *In vitro* release profile. *In vitro* NR release from the NR-NC formulation was examined using the dialysis bag diffusion method. Dialysis membranes (MWCO 12 000–14 000 Da, HiMedia, India) were pre-activated in distilled water for 12 hours at room temperature. NR dispersion and NR-NCs (equivalent to 5 mg of NR) were sealed in the dialysis bags and immersed in 100 ml of phosphate-buffered saline (pH 7.4 and pH 5.2 for comparative analysis) at 37 ± 0.5 °C with stirring (50 rpm). 1 ml of the sample was withdrawn at intervals up to 36 hours and replaced with fresh medium. All samples were stored at −20 °C and analysed using UV spectroscopy at 288 nm.[34–36] Release kinetics were assessed using the DD solver add-in for Microsoft Excel, and regression coefficients (R^2) were compared to determine the best fit.[37] In addition, a recovery study was performed by adding NR-NC samples at three concentration levels (2, 4 and 6 mg) to PBS (pH 5.2 and 7.4) and placing them in dialysis bags under the same conditions as the release experiment (37 °C, 24 h). Samples collected at 0 h and 36 h were analysed by UV spectrophotometry to determine the recoverable NR fraction.

3.4. Loading of NR-NCs in secondary vehicle (hydrogel)

Blank gel bases were fabricated by dispersing Carbopol-934P at varying concentrations of 0.5, 0.75, and 1% w/v, respectively, along with 0.25% w/v sodium alginate to utilise its adhesive property, in purified water under continuous stirring at 500 rpm for 5–6 hours at 25 °C. Triethanolamine was added to adjust the pH. The hydrogel base was then gradually combined with NR-NCs under constant agitation to incorporate the nano-carriers into the gel matrix.[38,39]

3.5. Characterisation of NR-NC-G

3.5.1. Rheological behaviour and texture analysis. The Anton Paar Rheometer MCR 302 was used to analyse the rheological behaviour of the various gels formulated. Based on this analysis, one concentration was selected as the final base for the nanocarrier. Numerous rheological tests have been conducted at 25 °C, including the determination of storage and loss moduli, frequency sweep examinations, amplitude sweep tests, shear stress *versus* shear strain measurements, and shear-dependent viscosity measurements. All results were compared with a commercially available anti-psoriatic hydrogel formulation containing clobetasol propionate.[31,40]

3.5.2. Appearance, pH and drug content uniformity. NR-NC-G has been examined for texture, colour, grittiness, odour, and phase separation. Consistency was assessed by compressing the formulated gel between two fingers. Furthermore, NR-NC-G (5 g) was weighed and diluted with warm water to a total volume of 20 mL. The mixture was then vigorously shaken for 1 minute. The pH was then measured, and readings were taken in triplicate.

To determine the drug content, 1 mL of gel was diluted with 10 mL of water in a measuring cylinder. The gel was then sampled from three distinct areas of the cylinder (top, middle, and bottom), and the drug content was estimated using a UV spectrophotometer.[1,41]

3.5.3. Antioxidant assays. 2,2-Diphenyl-1-picrylhydrazyl (DPPH) and hydrogen peroxide (H_2O_2) assays are commonly used to assess a compound's antioxidant potential, particularly in pharmaceutical and natural product research. DPPH assay evaluates the antioxidant capacity to neutralise the 2,2-diphenyl-1-picrylhydrazyl free radical, which has a rich purple hue and turns yellow when reduced.[42] The antioxidant activity

of NR-NC-G and bulk NR was assessed and compared to that of potent antioxidants, such as ascorbic acid and hydrogen peroxide, which served as positive controls in this experiment. All the samples produced above were added in triplicate to a 96-well plate. The blank was made of methanol. The prepared plate was incubated in the dark at 37 °C for 30 minutes. After incubation, the absorbance was recorded at 517 nm for the DPPH assay and at 230 nm for the H_2O_2 assay using a plate reader. The subsequent equation was used to compute the % scavenging activity.[43]

$$\text{Radical scavenging capacity}\,(\%) = \frac{A_0 - A}{A_0} \times 100 \qquad (2)$$

where A_0 is blank absorbance (DPPH solution) and A is absorbance of the sample.

3.5.4. Stability study. Stability testing aimed to examine the changes in the drug and physical characteristics of the formulation over time, particularly in response to variations in temperature and relative humidity. A comprehensive stability investigation was conducted over a three-month period, adhering to the ICH guidelines. NR-NC-G was subjected to different conditions: refrigerated at 4 ± 10 °C, normal at 25 °C ± 2 °C/60% ± 5% RH and accelerated at 40 °C ± 2 °C/75% ± 5% RH. Samples were withdrawn at 1, 2, and 3 months of the study for analysis.[27,44]

3.5.5. *Ex vivo* permeation. An *ex vivo* permeation study was performed on freshly excised skin (from the hairless abdomen region) of healthy BALB/c mice using a Franz diffusion cell.[45] The receptor compartment was filled with 20 mL of phosphate-buffered saline (PBS) at pH 7.4, while the drug solution and NR-NC-G (equivalent to 2.0 mg) were placed in the donor compartment. The mouse skin was then placed between the donor and receptor compartments. Then, the entire assembly was placed over the magnetic stirrer. The temperature was maintained at 37 ± 0.5 °C by circulating distilled water through the jacket of the receptor compartment while stirring the mixture at 50 rpm. Two millilitres of the sample were withdrawn from the donor compartment at various time intervals over a period of eight hours and replaced with the same quantity of PBS to maintain the sink condition. The samples were then examined using a UV-Visible spectrophotometer. The cumulative drug permeation through the skin was plotted against time, and the flux, J (mg cm^{-2} h^{-1}), was computed from the linear segment of the graph using the following equation.[46]

$$J = \partial m \;\div\; (A\;\partial t) \qquad (3)$$

where m is the cumulative amount of drug transported in t time, and A is the surface area of the skin (1.77 cm^2). The following equation determined the permeability coefficient (K_p):

$$K_p\ (\text{cm h}^{-1}) = J_{ss}/C_0 \qquad (4)$$

J_{ss} is the steady-state drug flux, and C_0 is the initial drug concentration in the donor cell.

3.5.6. Dermatokinetic study of NRG-NC-G. A similar experiment, like an *ex vivo* permeation study, was conducted, whereby drug concentration within various layers of the mouse skin was examined by applying the NR solution and NR-NC-G to the skin placed within a Franz diffusion cell.[47] Furthermore, in this experiment, the whole section of skin was removed from the cell at various time intervals. After rinsing the skin with a saline solution (pH 7.4), it was placed in hot water (2–4 minutes) to remove any traces of the drug or formulation from the skin. Furthermore, both layers (epidermis and dermis) were detached using forceps. These detached layers were finely sliced into small parts and placed in a methanol solution (2 mL) for 24 h to facilitate the extraction of NR and were quantified using HPLC.[31,48] $C_{skinmax}$ and AUC_{0-t} were determined using a non-compartmental analysis (NCA) approach.

3.5.7. *Ex vivo* skin toxicity and histological analysis. *Ex vivo* skin toxicity studies were conducted using freshly excised dorsal skin tissues obtained from BALB/c mice. Sections were cleaned with saline before being treated with NR solution and NR-NC-G, while the untreated skin served as a control. After eight hours, the sample was washed with distilled water and preserved in formalin. It was then sliced into five-micrometre-thick sections and stained with haematoxylin and eosin (H&E). Images were captured under a light microscope at 100× magnification.[49,50]

3.6. *In vitro* cell-line studies

The RAW 264.7 macrophage cell line was obtained from the National Centre for Cell Sciences (NCCS), Pune, India. Cells were cultured and maintained in DMEM supplemented with 10% fetal bovine serum, 1% antibiotic penicillin and streptomycin, cultured in a T-25 flask, and maintained at 37 °C in an incubator with 5% atmospheric CO_2 and observed daily. Bulk NR was dissolved in dimethyl sulfoxide (DMSO) and filtered through a 0.25 μm filter membrane. Samples were diluted in serum-free medium (SFM) to concentrations varying from 1000 to 31.25 μg mL^{-1}.[51]

3.6.1. MTT assay (cell viability). The cells were seeded in a 96-well plate (10 000 cells per well) and incubated for 24 h, then treated with varying concentrations of NR and NR-NC-G (as per test requirement, volume 100 μL in each well) and again incubated for 24 h and 48 h (as per test requirement). After completion of the incubation period, 3-(4,5-dimethylthiazol-2-yl)-2,5-diphenyltetrazolium bromide (MTT) solution (100 μL at a concentration of 5 mg mL^{-1}) was added to each well and further incubated for three hours. After the incubation period, the supernatant was discarded, and 100 μL DMSO was added to solubilise the formazan crystals. Finally, OD570 was measured on a microplate reader (BioTek Synergy H1, Agilent, U.S.) to evaluate the cell viability.[52]

3.6.2. Lipopolysaccharide (LPS) induced inflammation model. RAW 264.7 macrophages were seeded in 24-well plates at 10^5 cells per well and allowed to adhere overnight. The cells were treated with 1 μg mL^{-1} lipopolysaccharide (an inflam-

mation inducer) and incubated for an additional 24 hours. Successful activation of the inflammatory model was confirmed by the examination of the change in cell morphology.[53]

3.6.3. Anti-inflammatory activity and NO level estimation. RAW264.7 cells were initially treated with bulk NR and NR-NC-G at different concentrations ranging from 1000 to 31.25 μg mL^{-1} for two hours. Then, LPS (1 μg mL^{-1} in SFM) was added and incubated for an additional 24 hours. Furthermore, the NO amount was quantified with the Griess reagent using a slightly modified method prescribed previously.[51,54]

3.6.4. Cellular ROS assessment. A reactive oxygen species (ROS) assay was performed by using DCFDA, a cell-permeable fluorogenic dye that is deacetylated by the cellular esterases after it enters the cells in the form of a non-fluorescent compound; in the presence of intracellular ROS, it is subsequently oxidised to a bright green fluorescent product, *i.e.*, 2′,7′-dichlorofluorescein. RAW 264.7 cells were seeded at a density of 10 000 cells per well in 24-well plates for 24 h. Then, the cells were treated with bulk NR and NR-NC-G (125 μg mL^{-1}) for comparison. 1 μg mL^{-1} LPS was incorporated into the cells for two hours, and the cells were further incubated for 6, 12, and 24 hours. Untreated cells with 1 μg mL^{-1} LPS were kept as a positive control. The cells were washed twice with 1× PBS, and 20 μM DCF-DA was added. The cells were then incubated for 15 min at 37 °C in a CO_2 incubator. Finally, the DCF-DA solution was replaced with cold PBS, and fluorescence was examined using a fluorescence microscope (Leica DM3000, Germany) and a camera (DMC 5400, Leica, Germany). Digital images of each well were taken with a 20× objective using an image acquisition system (Leica Application Suite X (LAS X)).[54]

For quantification, the same experiment was run in a 96-well plate. ROS production was observed as an increase in the fluorescence intensity of the DCF dye, as measured at an excitation of 485 nm and an emission of 535 nm using a fluorescence plate reader.

3.6.5. Mitochondrial depolarisation study. Mitochondrial membrane potential ($\Delta\psi_m$), an indicator of mitochondrial dysfunction due to inflammation or protective effects of the formulations, was assessed using the fluorescent dye JC-1, following the protocol provided by the manufacturer. For the assessment, cells were incubated with the JC-1 staining solution for 10 min at 37 °C. LPS was employed as the positive control. After incubation, the cells were washed twice with JC-1 staining buffer to eliminate any excess dye or contaminants. The fluorescence of the stained cells was then visualised under a fluorescence microscope and measured using ImageJ image processing software. The green monomers and red aggregates signify changes in the mitochondrial membrane potential.[55,56]

3.7. Statistical analysis

Statistical analysis was performed using GraphPad Prism (GraphPad Software, San Diego, CA, USA). Following a significant effect examined by one-way or two-way analysis of variance (ANOVA), desirable multiple comparison tests were used to assess differences between group results. Tukey's Honest Significant Difference (HSD) test was used for all pairwise comparisons among group means to control the family-wise error rate. Sidak's multiple comparison test was employed for selected comparisons, offering improved statistical power compared to the Bonferroni method while maintaining control over type I error. Dunnett's test was particularly applied when comparing each treatment group to a single control, providing greater sensitivity by limiting the number of comparisons. All tests were conducted at a significance level of $\alpha = 0.05$, with corrections for multiple testing based on the chosen procedure.

4. Results

4.1. Analytical method development

A UV-Visible spectrophotometric analysis was done, and the λ_{max} of NR was observed at approximately 288 nm (Fig. S1a). It was observed that the absorbance increased linearly with concentrations ranging from 2 to 10 μg mL^{-1}, indicating good linearity.

For the HPLC analysis, the retention time for naringenin was found to be around 4.012 minutes (Fig. S1b), with a total run time of 7 minutes. The method was validated (SI data) and a calibration curve was established at concentrations ranging from 2 to 10 μg m^{-1} (Fig. S1c).

4.2. Optimisation of NR-LIPOs

At first, NR liposomes were optimised using a JMP custom design, and later, using the trapping method, NR-NCs were manufactured.[12] The trapping method employed was straightforward, economical, and rapid, proving ideal for preparing NCs as reported in the literature.

NR-LIPO optimisation was systematically approached using QbD principles as per ICH guidelines. Based on preliminary trials and risk analysis using an Ishikawa fishbone diagram (Fig. 1d), the amount of Lipoid-S-100 and cholesterol was a key CMA influencing the CQAs, specifically PS and %EE. A RSM design was employed to evaluate the effects and interactions of these CMAs, and second-order polynomial models were developed for both the responses. NR-LIPO is optimised through a systematic and statistical experimental approach integrating data from custom design, regression modelling (Table 2), graphical diagnostics (Fig. 2), and desirability-based optimisation. Ten experimental runs (Table 1) showed a wide distribution in PS, ranging from 167.9 to 298.2 nm, and EE, from 49.77% to 81.22%. The graph and linear equation trend suggested that an increase in Lipoid-S-100 and cholesterol concentrations is directly proportional to a rise in particle size and a concurrent decline in %EE, which may be due to limitations in the formation and entrapment of multilamellar vesicles.

Table 2 summarises the model's statistical performance, showing excellent fit, with R^2 values of 0.9894 for PS and

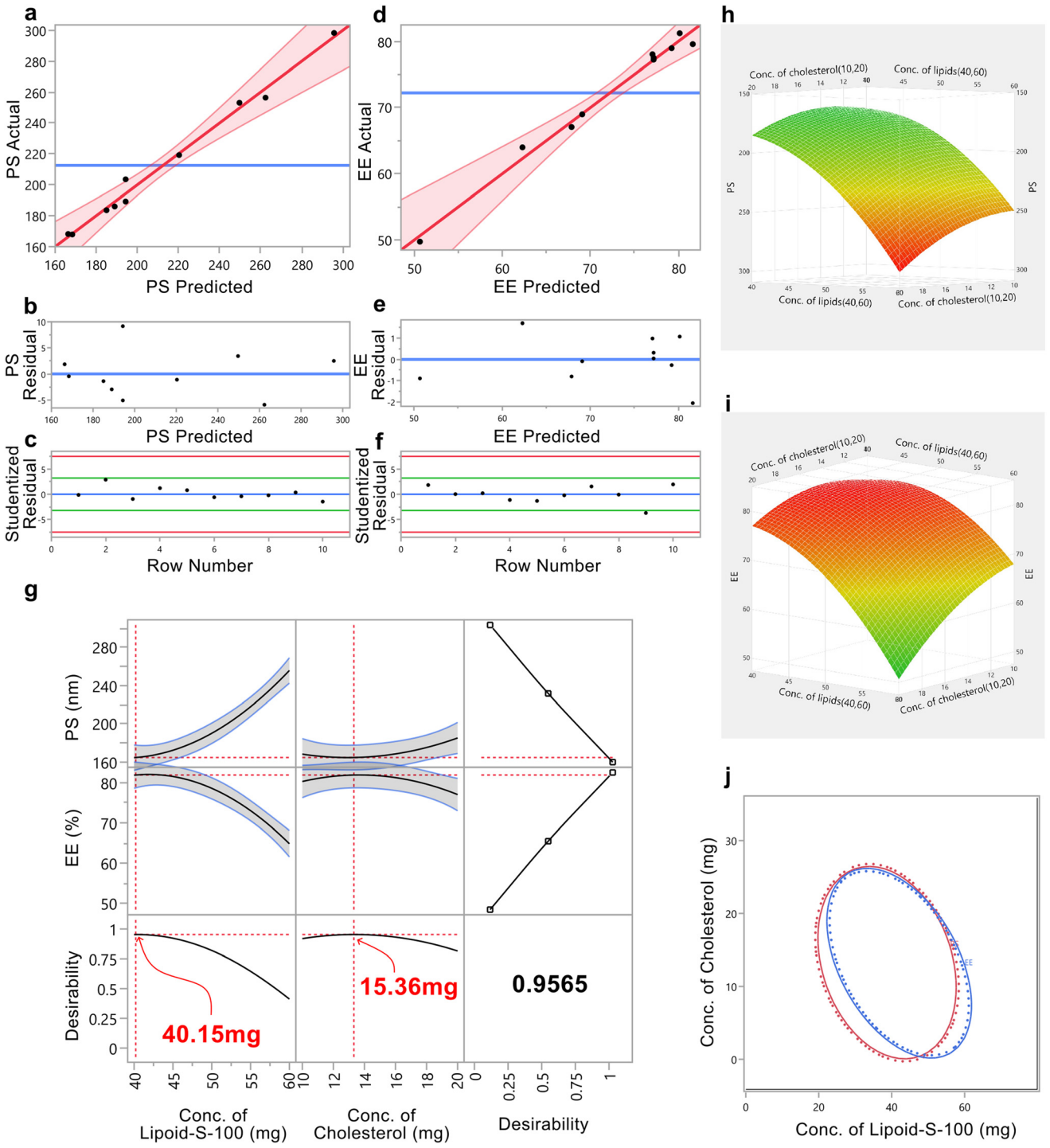

Fig. 2 Model diagnostics and response surface optimisation for the NR-LIPO formulation. (a and d) Actual *versus* predicted plots for particle size (PS) and encapsulation efficiency (EE), demonstrating strong linear correlation. (b, c, e and f) Residual and normal probability plots confirming homoscedasticity and the normal distribution of errors. (h and i) Three-dimensional surface plots illustrating the effects of lipid and cholesterol concentrations on PS and EE. (g) Desirability function identifying the optimal formulation at 40.15 mg Lipoid-S-100 and 15.36 mg cholesterol. (j) Overlay contour plot delineating the design space for the simultaneous optimisation of PS and EE.

0.9875 for %EE, and adjusted R^2 values of 0.9763 and 0.9720, respectively. The lower RMSE values, *i.e.*, 6.70 for PS and 1.65 for EE, again supported the precision of the model. The statistical significance of both models ($p < 0.001$) was confirmed by ANOVA, and high *F*-ratios (75.23 for PS and 63.54 for %EE) were found, which indicates that the chosen variables are responsible for most of the variability in the responses. The regression equations found for each response quantify the

Table 1 Experimental design and results for NR-LIPO development

Components of NR-LIPO				
Independent variables and their levels				
Component	Unit	Low (−1)	Mid (0)	High (+1)
Lipoid S100 (X_1)	mg	40	50	60
Cholesterol (X_2)	mg	10	15	20
Dependent variables and their constraints				
Particle size (Y_1)	nm	Minimized		
Encapsulation efficiency (Y_2)	%	Maximized		

Design space of NR-LIPO using custom design, limiting trials to 10 runs

Run no.	X_1	X_2	Y_1	Y_2
NR-LIPO1	40	10	167.9 ± 2.5	81.22 ± 1.25
NR-LIPO2	50	15	203.5 ± 1.25	77.23 ± 2
NR-LIPO3	50	15	189.2 ± 3.45	77.5 ± 3.65
NR-LIPO4	60	10	253.1 ± 10.25	67.07 ± 2.11
NR-LIPO5	60	20	298.2 ± 12.35	49.77 ± 2.5
NR-LIPO6	50	10	186 ± 5.36	78.96 ± 3.5
NR-LIPO7	40	20	183.6 ± 5.23	78.04 ± 3.15
NR-LIPO8	50	20	219.2 ± 3.65	68.99 ± 1.25
NR-LIPO9	40	15	168.2 ± 4.23	79.57 ± 3.5
NR-LIPO10	60	15	256.4 ± 3.25	64 ± 2.5

All runs were conducted in triplicate (n = 3).

influence of linear, quadratic, and interactive effects of independent variables:

$$\mathrm{PS} = 194.31 + 48X_1 + 20.04{X_1}^2 + 15.67X_2 + 10.34{X_2}^2 + 7.35X_1X_2 \quad (5)$$

$$\%\,\mathrm{EE} = 77.19 - 9.67X_1 - 5.08X_2 - 5.22{X_1}^2 - 3.53X_1X_2 - 3.03{X_2}^2 \quad (6)$$

Graphical evaluation of the statistical models through diagnostic and response surface figures validated the significance of using models to understand formulation behaviour. The actual *versus* predicted plots (Fig. 2a and d) for both PS and % EE showed strong linear correlation, with data points closely aligned along the diagonal, proving that the regression models correctly predicted experimental outcomes. These findings are further supported by the residual *versus* predicted plots (Fig. 2b and e), which show a random scatter of residuals around zero, confirming that the models met the assumption of homoscedasticity and were free from systematic bias. The 3D response surface (Fig. 2h and i) visually represented the interaction between Lipoid-S-100 and cholesterol. For PS, both variables exhibited a synergistic effect, with increases in either leading to larger vesicles, which may be due to multilamellar vesicle formation and thickness in lipidic layers. In contrast, for %EE, an antagonistic effect was seen; higher Lipoid-S-100 and cholesterol levels led to reduced drug entrapment, potentially due to saturation of the lipid matrix in liposomal vesicles. These opposing trends highlighted the need for a balanced formulation strategy. The desirability plot (Fig. 2g) further integrated these findings by identifying an optimal region in the design space that satisfies both response criteria.

The contour overlay plot (Fig. 2j) represents the design space optimisation of NR-LIPO, based on two CQAs: PS and % EE, and plotted against the concentrations of Lipoid-S-100 on the x-axis and cholesterol on the y-axis. The red contour represents the response surface for PS, where the red dotted region indicates areas that meet the condition of minimised particle size. The blue contour corresponds to %EE, showing

Table 2 Statistical model summary and optimal conditions for NR-LIPO

Summary of fit				
Response	R^2	Adjusted R^2	RMSE	MR
Y_1	0.9894	0.9763	6.7026	212.53
Y_2	0.9875	0.9720	1.6500	72.235

ANOVA						
Parameters	DF	SS	MS	F-Ratio	p-Value	Model significance
Y_1						
Model	5	16 898.240	3379.65	75.2282	0.0005	Significant
Error	4	179.701	44.93	—	—	—
C. total	9	17 077.941	—	—	—	—
Y_2						
Model	5	864.934	172.987	63.5353	0.0007	Significant
Error	4	10.890	2.723	—	—	—
C. total	9	875.825	—	—	—	—

Optimal values, desirability search approach					
Sample	X_1	X_2	Y_1	Y_2	Desirability
NR-LIPO11	40.15	13.36	164.81	81.83	0.9565

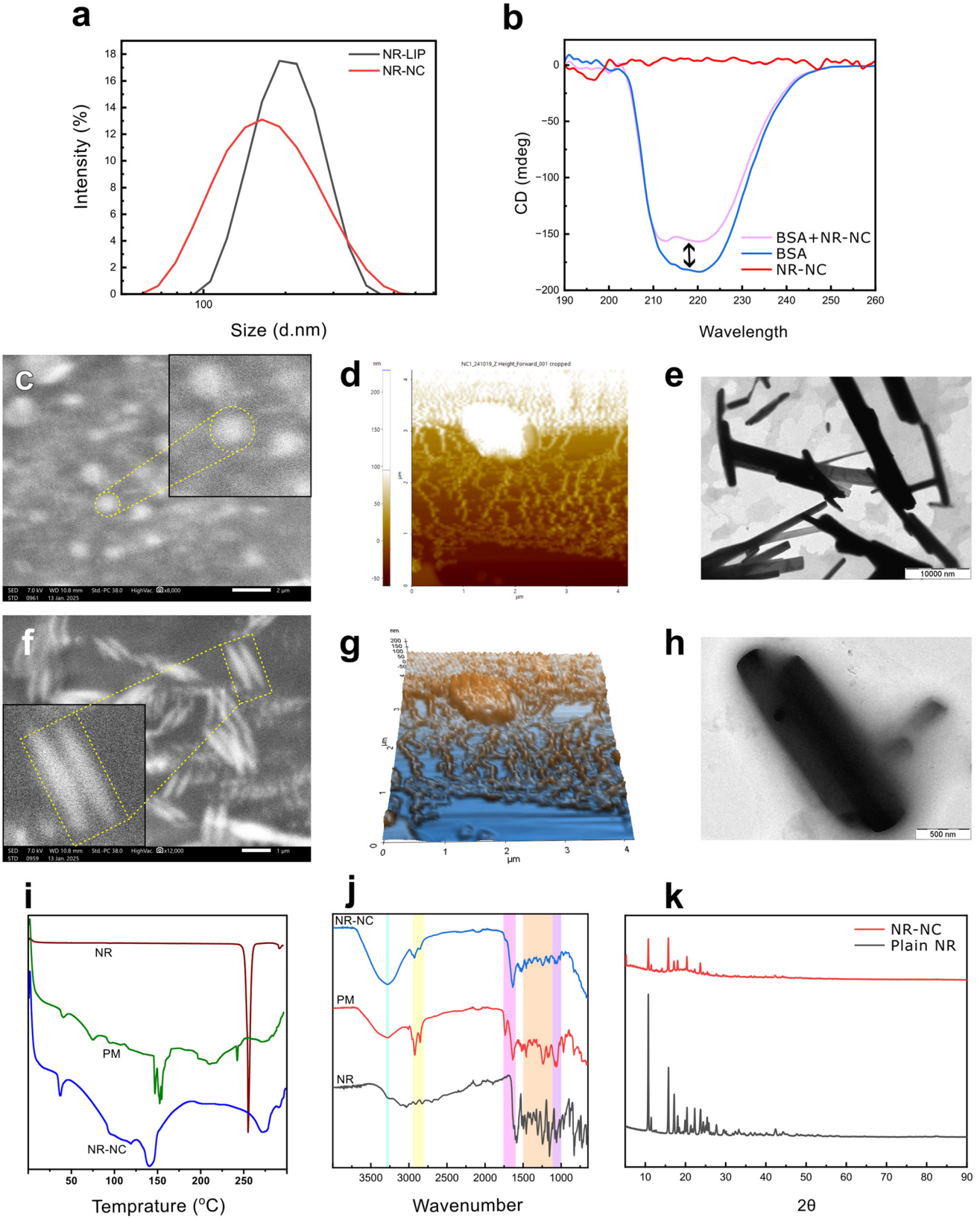

Fig. 3 (a) DLS profiles of NR-LIPO and NR-NC, confirming particle size distribution following calcium-induced transformation; (b) CD spectra depicting secondary structural alterations in BSA and NR-NC; (c) SEM image of NR-LIPO11; (d and g) AFM images illustrating the three-dimensional topography and structural organisation of NR-NC; (e and h) TEM images of NR-NC, revealing elongated, rod-like cylindrical structures; (f) SEM image of NR-NCs; (i) DSC thermograms of pure NR, physical mixture, and NR-NC; (j) ATR spectra of pure NR, physical mixture, and NR-NC; (k) XRD spectra of NR and NR-NCs.

areas where %EE is maximised or within the desirable range. The overlapping region between the red and blue contour lines signifies the "sweet spot or design space". This area is an optimal space where a combination of Lipoid-S-100 and cholesterol concentrations simultaneously satisfies both response criteria: minimising the PS and optimum or high %EE. The desirable design space is relatively confined, emphasising that only specific ranges of Lipoid-S-100 (around 40–50 mg) and cholesterol (around 10–15 mg) allow both criteria to be met. It is found that outside the design space, you either get too large particles or inadequate EE.

The desirability function analysis (Fig. 2g) enabled simultaneous optimisation of both responses. An optimal formulation (NR-LIPO11) was identified, yielding a predicted particle size of 164.81 nm, a %EE of 81.83%, and a desirability score of 0.9565. This solution falls within the robust design space, as confirmed by the overlaid contour plots, indicating a favourable balance between particle size and drug loading efficiency.

4.3. Transformation and stabilisation of NR-LIPO into NR-NCs

The amount of $CaCl_2$ and BSA, used as aggregation inhibitors, was optimised using DLS and CD spectroscopy. DLS was employed to identify the transformation of liposomes into nanocochleates by assessing changes in particle size distribution. The intensity-weighted size distribution curves revealed a distinct flattening, attributed to calcium-induced structural reorganisation. The NR-LIPO11 formulation exhibited a sharp, narrow peak at around 164 nm, indicating a relatively uniform liposome population. Conversely, the NR-NCs exhibited a broader size distribution (Fig. 3a). This flattening of the curve was interpreted as confirmation of the successful transition from liposomes to nanocochleates, mediated by the addition of calcium chloride.

CD spectra were utilised to provide critical insights into the structural alterations of BSA upon interaction with NCs. The spectrum of pure BSA (Fig. 3b, blue) exhibited a prominent negative peak at around 210–220 nm, characteristic of a predominant α-helical structure, consistent with the secondary composition of 18.7% α-helix and 58.7% β-sheet. In contradiction, NCs alone (red line) showed no significant CD signal, confirming the absence of intrinsic secondary structures. On addition of BSA in NCs (pink), a decrease in ellipticity was observed, which indicates structural modifications. This change correlated with an increase in α-helical content from 18.7% to 31.6%, an increase in β-sheets from 58.7% to 66.4%, and a marked reduction in disordered structures from 19.9% to 2.0%. These conformational changes suggested that BSA underwent structural tightening, likely driven by hydrophobic and electrostatic interactions with NCs. Based on these observations, the final optimised NR-NC formulation was achieved by adding 0.1 mM (500 μL) calcium chloride and 60 μg mL^{-1} (1.2 mL) BSA to the NR-LIPO11 system.

4.4. Characterisation of NR-NCs

The HD of the NR-NCs was within the nanoscale range, specifically 168 ± 1.8 nm. Additionally, the PDI was found to be 0.25, indicating a highly uniform PSD. The ζ-potential of 26.6 ± 1.6 mV indicates a moderately charged surface capable of providing electrostatic repulsion; additionally, the BSA coating contributes steric stabilisation, collectively ensuring adequate colloidal stability and minimising aggregation of the nanocochleates. The %EE of the optimised NR-NCs was evaluated using a centrifugation method, yielding a value of 85.23 ± 4.33%. This high EE indicates effective encapsulation of NR within the nanocochleate structures.

Morphological SEM analysis revealed that liposomes exhibited smooth, spherical vesicular structures, as shown in Fig. 3c. In contrast, NR-NCs displayed elongated, cylindrical morphologies (Fig. 3f), indicating a successful structural transformation induced by calcium interaction. Zoomed-in micrographs emphasised the uniformity and structural integrity of these rod-like particles. AFM images (Fig. 3d and g) further confirmed the rod-shaped morphology, with topographic height profiles ranging between 135 and 150 nm, consistent with nanoscale dimensions.

TEM images provided a detailed visualisation of the internal lamellar organisation of the NR-NCs. Fig. 3e shows densely packed elongated rods, whereas Fig. 3h depicts an individual, well-defined nanocochleate, clearly revealing the characteristic rolled lipid bilayer architecture.

4.4.1. Thermal analysis. The DSC thermogram (Fig. 3i) shows the thermal behaviour of pure NR, the physical mixture (PM), and the final nanocarrier formulation (NR-NC). NR reveals a sharp endothermic peak at around 245 °C, corresponding to its melting point and indicating its crystalline nature. In the PM, the NR melting peak is significantly reduced and broadened; this may be due to a smaller amount of drug in PM. In the NR-NC, there is a complete disappearance of the NR peak, indicating successful entrapment and molecular dispersion within the carrier.

4.4.2. Attenuated total reflectance infrared spectroscopy (ATR-IR). Potential interactions between the NR and excipients were analysed, and it was found that pure NR (Fig. 3j, black) showed characteristic peaks, particularly broad O–H stretching at around 3400 cm^{-1}, C═O stretching near 1650 cm^{-1}, and aromatic C═C vibrations between 1600 and 1400 cm^{-1}. These confirmations indicate the presence of phenolic and flavonoid structures in NR. In PM (Fig. 3j, red), notable shifts and intensity loss are observed; these bands suggest intermolecular interactions, such as hydrogen bonding and hydrophobic interactions, especially involving the carbonyl and hydroxyl groups of NR with Lipoid-S-100 and BSA. The appearance of additional bands or shifts near 2900 cm^{-1} (aliphatic C–H stretching) and 1500–1000 cm^{-1} (fingerprint region) is due to Lipoid-S-100 and BSA. In the case of NR-NCs (Fig. 3j, blue), suppression or displacement of NR original peaks and the appearance of new band patterns, especially in the 1500–1000 cm^{-1} range, strongly suggest successful encapsulation. An effective encapsulation of NR within the nanocochleate matrix, without any chemical degradation, is confirmed by the results obtained.

4.4.3. Powder X-ray diffraction. Fig. 3k represents the X-ray diffractograms of NR and NR-NCs. NR showed high intensity

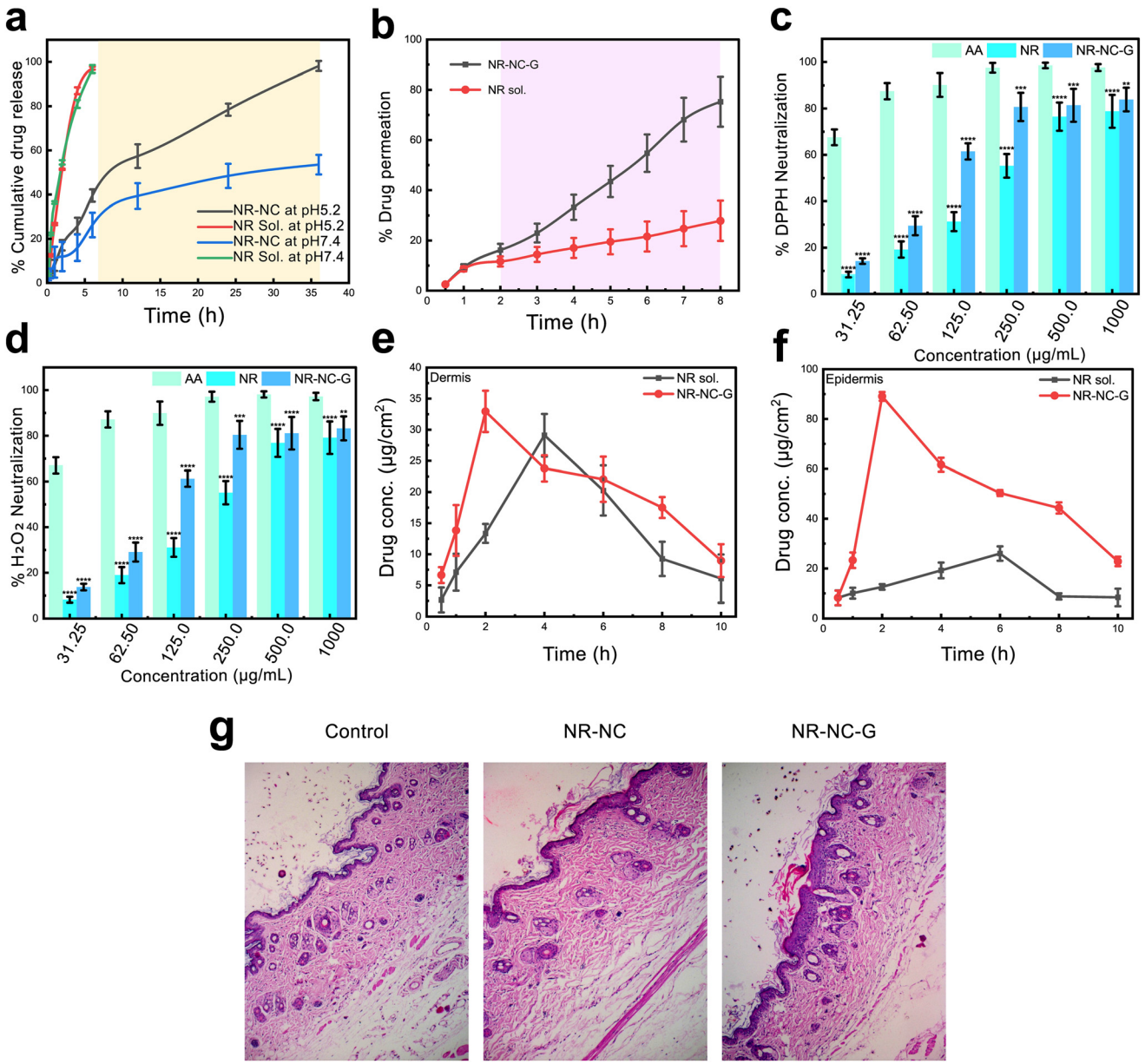

Fig. 4 (a) *In vitro* drug release at pH 5.2 and 7.4; (b) percentage permeation of NR-NC-G compared to NR solution; (c and d) H_2O_2 and DPPH assays demonstrating enhanced antioxidant activity of NR-NC-G relative to NR (statistical comparisons were performed using Tukey's multiple comparison test. Significance levels are indicated as follows: ****$p < 0.0001$, **$p = 0.0014$, *$p = 0.0180$, relative to the AA group); (e and f) comparative analysis of epidermal and dermal drug concentrations following treatment with NR-NC-G *versus* NR solution; and (g) histological images showing standard skin architecture in the control group, preserved epidermis in the NR-NC-G group, and mild alterations in NR-NC-treated tissue.

sharp diffraction peaks at (2θ) angles of 10.74°, 15.7°, 17.14°, 20.38°, and 22.31°, showing its ordered crystalline nature. In contrast, the NR-NCs showed some sharp peaks with a lower intensity, clearly demonstrating successful encapsulation of NR in nanocochleates.

4.4.4. *In vitro* drug release. The drug release behaviour observed using different pH environments reveals a clear difference in performance between the NR solution and NR-NCs. The NR solution shows a complete release of the drug within 6–7 hours at both pH 5.2 and pH 7.4 (Fig. 4a). The recovery values for all concentration levels ranged from 99% to 101%, confirming that neither NR degradation nor dialysis membrane adsorption interfered with the quantification method. It is observed that NR-NCs exhibit a sustained release, which is highly pH-dependent, as highlighted in the yellow-coloured region. At pH 5.2, the drug is released steadily, reaching complete release by 36 hours. However, at pH 7.4, the release is slower and reaches approximately 55% by the end of 36 hours. The obtained release patterns are strongly supported by the statistical models applied. At pH 5.2, NR-NCs follow a first-order

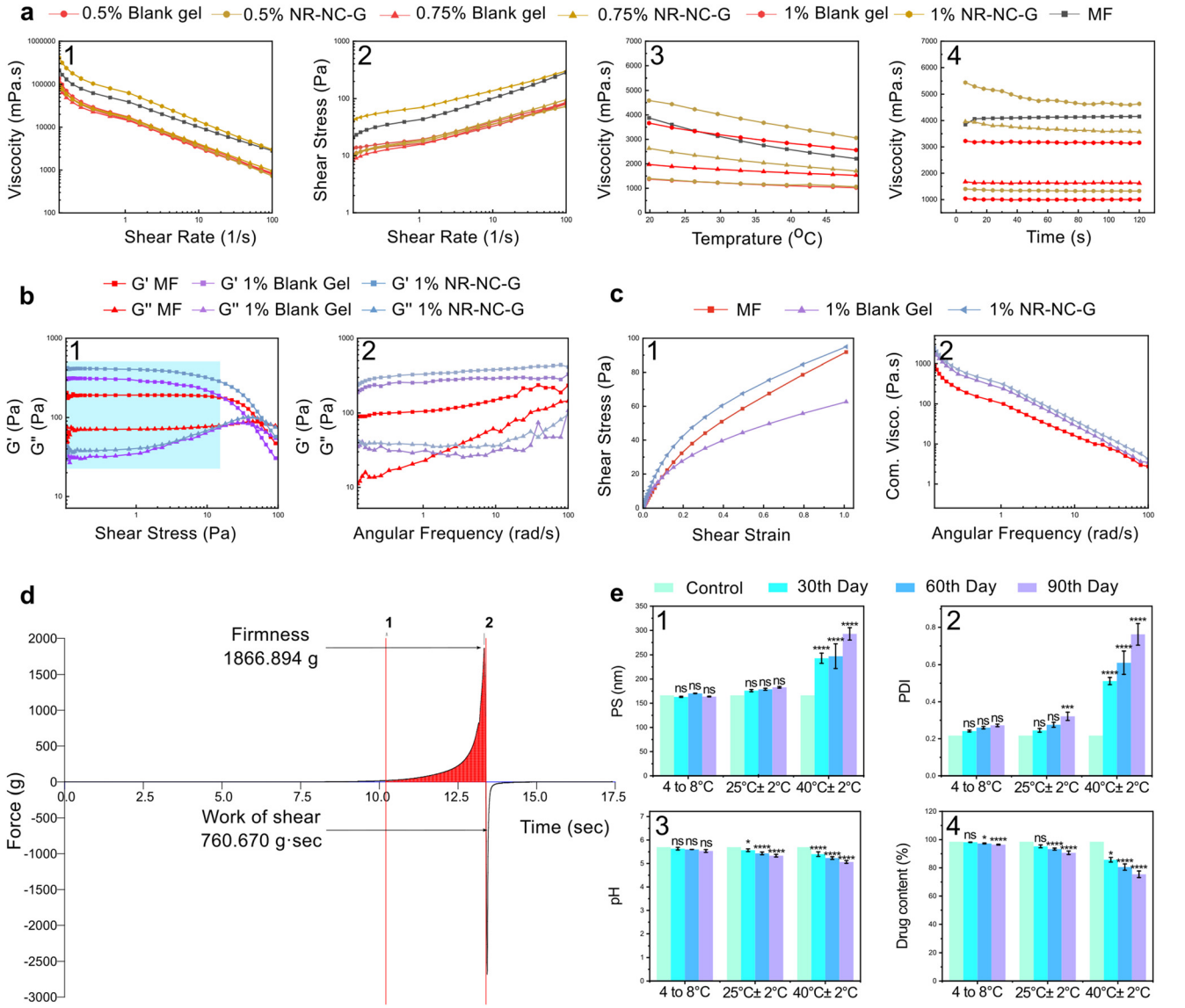

Fig. 5 Rheological and stability evaluation of NR-NC-G. (a) Shear-thinning and pseudoplastic behavior demonstrated through viscosity *versus* shear rate, shear stress, time, and temperature plots; (b) amplitude and frequency sweep profiles of NR-NC-G, blank gel, and MF; (c) shear strain and complex viscosity plots confirming mechanical robustness; (d) texture analysis profile of NR-NC-G; and (e) stability assessment over three months, evaluating particle size, pH, and drug content under refrigerated conditions (statistical comparisons were performed using Tukey's multiple comparison test. Significance levels are indicated as follows: ****$p < 0.0001$, ns = 0.9448, relative to the control group).

model with an adjusted R^2 of 0.9922, indicating excellent correlation between the obtained data and the model. The Akaike Information Criteria (AIC) value of 40.8162 is the lowest among all models tested for this condition, reinforcing that this model offers the best trade-off between goodness of fit and model complexity. Additionally, the Model Selection Criterion (MSC) value of 4.6303 signifies a statistically robust model with high predictive accuracy. This aligns with the observed continued and consistent release, as the system maintains concentration-driven diffusion over time. These values confirm that model selection accurately reflects the underlying transport mechanisms, with pH playing a crucial role in modulating release kinetics, particularly over extended durations.

4.5. Characterisation of NR-NC-G

Based on rheological evaluation and matching with the marketed formulation (MF), the optimum concentration of the gel formulation was selected to ensure desirable properties of the gel formulation. The results obtained from various gel formulations, including blank gels and NR-NC-G, showed that 1% NR-NC-G in Carbopol 934P gel exhibited superior physicochemical behaviour, making it the optimal choice for further development.

4.5.1. Rheological behaviour. In the viscosity flow curve analysis at the shear rate gradient profile (Fig. 5a-1), all formulations followed shear-thinning behaviour, which is desirable

for topical applications. Specifically, 1% NR-NC-G maintained a higher viscosity across all shear rates compared to its corresponding blank gel and was found to be superior to the marketed antipsoriatic hydrogel (MF), indicating good structural integrity at rest and ease of spreadability under shear. The shear stress *versus* shear rate graph (Fig. 5a-2) further confirmed the pseudoplasticity of 1% NR-NC-G, characterised by a nonlinear increase in shear stress with increasing shear rate. This signifies a strong internal gel network capable of resisting deformation and supporting structural recovery post-application. In the time-dependent viscosity study (Fig. 5a-4), 1% NR-NC-G exhibited moderate thixotropy, with only a slight decline in viscosity over time, while maintaining greater stability than the corresponding blank gel and aligning closely with MF. Furthermore, the temperature-dependent viscosity profile (Fig. 5a-3) showed that 1% Carbopol 934P containing NR-NC-G retained its viscosity consistently across a temperature range of 20–50 °C, confirming its thermal stability and robustness under varying environmental conditions. Altogether, the selection of the 1% NR-NC-G formulation was justified based on Fig. 5a-1–4.

In Fig. 5b-1, blank gel, NR-NC-G and MF exhibited a wide linear viscoelastic region (LVER) (marked in the blue background) in the plot, suggesting good internal network stability under low applied stress. However, NR-NC-G demonstrated a higher G', indicating a more dominant elastic character. This signifies improved structural rigidity, a critical factor for maintaining the formulation's shape and mechanical integrity during application and storage.

Furthermore, the viscoelastic nature was examined through frequency sweep measurements, as illustrated in Fig. 5b-2. Both G' and G'' remained consistent across the tested angular frequency range, verifying frequency-independent behaviour—an indication of a robust gel network. NR-NC-G consistently shows higher G' values than MF, reinforcing its superior elastic nature. The inclusion of NR-NCs into the gel did not alter this profile, certifying that NR-NCs were well integrated within the gel matrix. This demonstrates excellent mechanical stability of the hydrogel, even after incorporating the nanocarrier.

Shear stress *versus* shear strain was examined to evaluate deformation behaviour, as shown in Fig. 5c-1. A nonlinear increase in shear strain with increasing shear stress was observed, indicating pseudo-plastic behaviour. This property is particularly favourable for topical applications, as it suggests that the formulation remains strong under static conditions but becomes more fluid under mechanical stress, ensuring easy application without compromising retention.

Lastly, the complex viscosity *versus* angular frequency was analysed (see Fig. 5c-2). The viscosity of NR-NC-G was higher than that of MF and showed a decreasing trend with increasing frequency, confirming its shear-thinning nature. High viscosity is often associated with enhanced mucoadhesion. Together, these characteristics indicate that the formulation combines mechanical robustness.

From texture analysis (Fig. 5d), it was found that NR-NC-G has a firmness value of 1866.894 g and a work of shear of 760.670 g s. This indicates that the gel has a moderate level of hardness and a moderate energy requirement for spreading the gel, respectively. According to the results, the gel has sufficient structural integrity while remaining easy to apply.

4.5.2. Appearance, pH and drug content uniformity. Along with perfect rheological behaviour, NR-NC-G exhibited excellent physical characteristics. The organoleptic evaluation confirmed that the gel has an acceptable greasiness, a soft white colour, a pleasant odour, and a smooth texture, with no visible phase separation, indicating good physical stability. Upon manual compression of NR-NC-G between the fingers, it is observed that the gel has a uniform and satisfactory texture.

The pH of the gel was found to be in the range of 5.0 to 5.5, which is compatible with the natural pH of the skin. Drug content analysis based on samples taken from the top, middle, and bottom of the gel showed values of 99.21%, 98.78%, and 97.32%, respectively. These results indicate good uniformity in the drug content of NR-NC-G.

4.5.3. Antioxidant assays. The H_2O_2 assay (Fig. 4d) results demonstrated that NR showed a high IC_{50} value of 185.05 μg mL^{-1}, indicating lower antioxidant potency. On the opposite side, NR-NC-G showed significantly enhanced antioxidant potential with a lower IC_{50} value of 91.84 μg mL^{-1}. Statistical analysis revealed that NR differed significantly from hydrogen peroxide at all concentrations (****$p < 0.0001$), while NR-NC-G showed reduced significance at higher doses (*$p = 0.0180$ at 500 μg mL^{-1}; ns = 0.2505 at 1000 μg mL^{-1}), indicating dose-dependent antioxidant efficacy of NR-NC-G.

The same trend was observed in the DPPH neutralisation assay (Fig. 4c). The IC_{50} of NR was 183.71 μg mL^{-1}, while NR-NC-G again exhibited stronger activity with an IC_{50} value of 92.12 μg mL^{-1}. Ascorbic acid (AA), as expected, showed the highest efficacy. Tukey's *post hoc* test indicated that NR remained significantly different from AA at all concentrations (****$p < 0.0001$), whereas NR-NC-G showed non-significant differences at higher concentrations (ns = 0.3394 at 1000 μg mL^{-1}; **$p = 0.0014$ at 500 μg mL^{-1}), further supporting its improved functional performance. These results confirm that the entrapment of NR into the nano-complex formulation substantially enhances its antioxidant potential, highlighting its promise for applications in targeting oxidative stress.

4.5.4. Stability study. The stability studies of the NR-NC and its gel formulation (NR-NC-G) are shown in Fig. 5e. The NR-NCs exhibited minimal changes in PS and PDI under refrigerated conditions (4–8 °C), as indicated by the consistent bar heights, which showed PS close to 170–180 nm and PDI below 0.5 (Fig. 5e-1 and e-2). ANOVA analysis revealed no statistically significant changes in the study parameters. Under normal storage conditions of 25 °C ± 2 °C/60% ± 5% RH, a slight increase in PS and PDI was observed, while accelerated conditions (40 °C ± 2 °C/75% ± 5% RH) showed increased PS and PDI, which may be due to the aggregation of NR-NCs. For NR-NC-G, the pH and drug content remained stable under refrigerated conditions, as indicated by the steady bars showing pH around 5.2–5.5 and drug content within the limit of 90–100% (Fig. 5e-3 and e-4), whereas accelerated conditions

resulted in slight reductions in drug content and minor pH fluctuations. These results, as shown in Fig. 5e, indicate that refrigerated storage ensures optimal stability for NR-NC-G, thereby maintaining its structural integrity.

4.5.5. *Ex vivo* permeation. As shown in Fig. 4b, over an 8-hour period, NR-NC-G achieved nearly 90% drug permeation, whereas the NR solution permeated only about 35%. This enhanced permeation is attributed solely to the nanocarrier-based gel, which facilitates deeper penetration of NR-NCs through the skin layers. The gel matrix may act as a reservoir, constantly delivering the drug to the diseased site; in contrast, the NR solution lacks such a mechanism.

This enhanced performance is further validated by quantitative permeation metrics. The flux of NR-NC-G was significantly higher at 5.960 μg cm^{-2} h^{-1}, as compared to 0.410 μg cm^{-2} h^{-1} for the NR solution—showing nearly a 15-fold increase in drug transport efficiency. In addition to this, the permeability coefficient of NR-NC-G (2.980 cm h^{-1}) is markedly higher than that of the NR solution (0.205 cm h^{-1}), confirming the formulation's superior skin permeation capacity. Altogether, these results highlight the potential of NR-NC-G as a highly effective topical drug delivery system for enhancing the bioavailability of poorly soluble compounds, such as naringenin, offering a highly permeable dosage formulation for dermal administration.

4.5.6. Dermatokinetic study of NRG-NC-G. The dermatokinetic study was performed to compare the skin distribution behaviour of NR from NR-Sol and NR-NC-G, with particular focus on drug accumulation and retention in the epidermis and dermis layers of skin. The data, presented in Fig. 4e and f and Table 3, provide a detailed overview of the dermatokinetic parameters that support the enhanced topical delivery potential of NR-NC-G, specifically in the context of treating chronic dermatological conditions, such as psoriasis.

In the dermis, NR-NC-G exhibited faster drug absorption, with a $T_{skinmax}$ of 2 hours, compared to 4 hours for NR-Sol. The maximum dermal concentration ($C_{skinmax}$) achieved with NR-NC-G was 32.94 ± 3.32 μg cm^{-2}, higher than that of NR-Sol (29.11 ± 3.42 μg cm^{-2}). Another important factor, AUC_{0-t}, which reflects cumulative drug exposure, was significantly greater for NR-NC-G (198.78 ± 26.12 μg h cm^{-2}) than for NR-Sol (149.99 ± 29.77 μg h cm^{-2}), suggesting more efficient drug deposition. The lower elimination rate constant (K_e) for NR-NC-G (0.17 ± 0.03 h^{-1}) compared to NR-Sol (0.33 ± 0.15 h^{-1}) further supports the slower clearance of NR-NC-G from the dermal compartment.

Table 3 Comparative dermatokinetic data of NR-Sol and NR-NC-G

	NR-Sol (dermis)	NR-NC-G (dermis)	NR-Sol (epidermis)	NR-NC-G (epidermis)
$T_{skinmax}$ (h)	4	2	6	2
$C_{skinmax}$ (μg cm^{-2})	29.11 ± 3.42	32.94 ± 3.32	26.00 ± 2.90	89.07 ± 1.76
AUC_{0-t}	149.99 ± 29.77	198.78 ± 26.12	147.01 ± 22.74	490.59 ± 20.73
K_e	0.33 ± 0.15	0.17 ± 0.03	0.30 ± 0.08	0.15 ± 0.01

The differences were even more significant in the epidermis, the primary target site for therapeutic action in psoriasis. Both NR sol. and NR-NC-G reached high epidermal concentration at 2 hours, but NR-NC-G achieved a markedly higher $C_{skinmax}$ of 89.07 ± 1.76 μg cm^{-2}, compared to NR-Sol. The AUC_{0-t} for NR-NC-G in the epidermis was 490.59 ± 20.73 μg h cm^{-2}, over threefold higher than that of NR-Sol. Similarly, the K_e for NR-NC-G was significantly lower (0.15 ± 0.01 h^{-1}) than for NR-Sol, indicating that NR-NC-G has the ability to retain the drug longer in the skin.

4.5.7. *Ex vivo* skin toxicity and histological analysis. Histological analysis of the *ex vivo* dorsal skin sections stained with H&E showed significant differences in tissue response in the three groups (Fig. 4g). The control group exhibited normal skin architecture, characterised by a well-structured, stratified epidermis and intact dermal connective tissue, providing a baseline for comparison. In the NR-NC-treated skin tissue, a slight reduction in epidermal thickness and a moderate alteration in the dermal structure are evident, possibly indicating a mild irritant effect due to the nanoformulation. In contrast, NR-NC-G demonstrates a preserved epidermal structure and organised dermal layers, suggesting that improved tissue compatibility and reduced irritancy may be due to the water-based gel formulation. The histological examination was performed under blinded conditions; these morphological differences are interpreted as treatment-specific effects. Finally, NR-NC-G appears to offer potential suitability for topical or transdermal applications.

4.5.8. Therapeutic effects of NR-NC-G on LPS-stimulated RAW264.7 cells. To evaluate the cytocompatibility of NR-NC-G compared to bulk NR and placebo NC-G, RAW264.7 macrophages were incubated with increasing concentrations (31.25 to 1000 μg mL^{-1}), and percent cell viability was assessed after 24 hours. The results revealed a significant increase in cell viability in NR-NC-G-treated cells compared to those treated with bulk NR at all concentrations tested (Fig. 6a). For instance, at the highest dose of 1000 μg mL^{-1}, NR-NC-G maintained a viability of ~21.3%, compared to only 4.3% for NR ($p < 0.0001$). In contrast, the blank NC-G group exhibited biocompatibility, with a viability of ~96.1%. Similar trends were observed at 500 μg mL^{-1}. Importantly, at 250 μg mL^{-1}, NR-NC-G preserved a significantly higher viability, while that of NR-treated cells dropped to ~33.1% ($p < 0.0001$), highlighting the safe and biocompatible profile of NR-NC-G at therapeutic concentrations.

As the concentration decreased, the protective effect of NR-NC-G remained statistically significant but was less pronounced. At 125 and 62.5 μg mL^{-1}, NR-NC-G-treated cells maintained high cell viability percentages, outperforming the bulk NR. Collectively, these findings clearly demonstrate that NR maintained over 50% cell viability up to a concentration of 213.33 μg mL^{-1}, while NR-NC-G exhibited similar tolerance up to 432.58 μg mL^{-1} and below these concentrations, the reduction in cell viability was not statistically significant compared to control, suggesting relatively high biocompatibility at

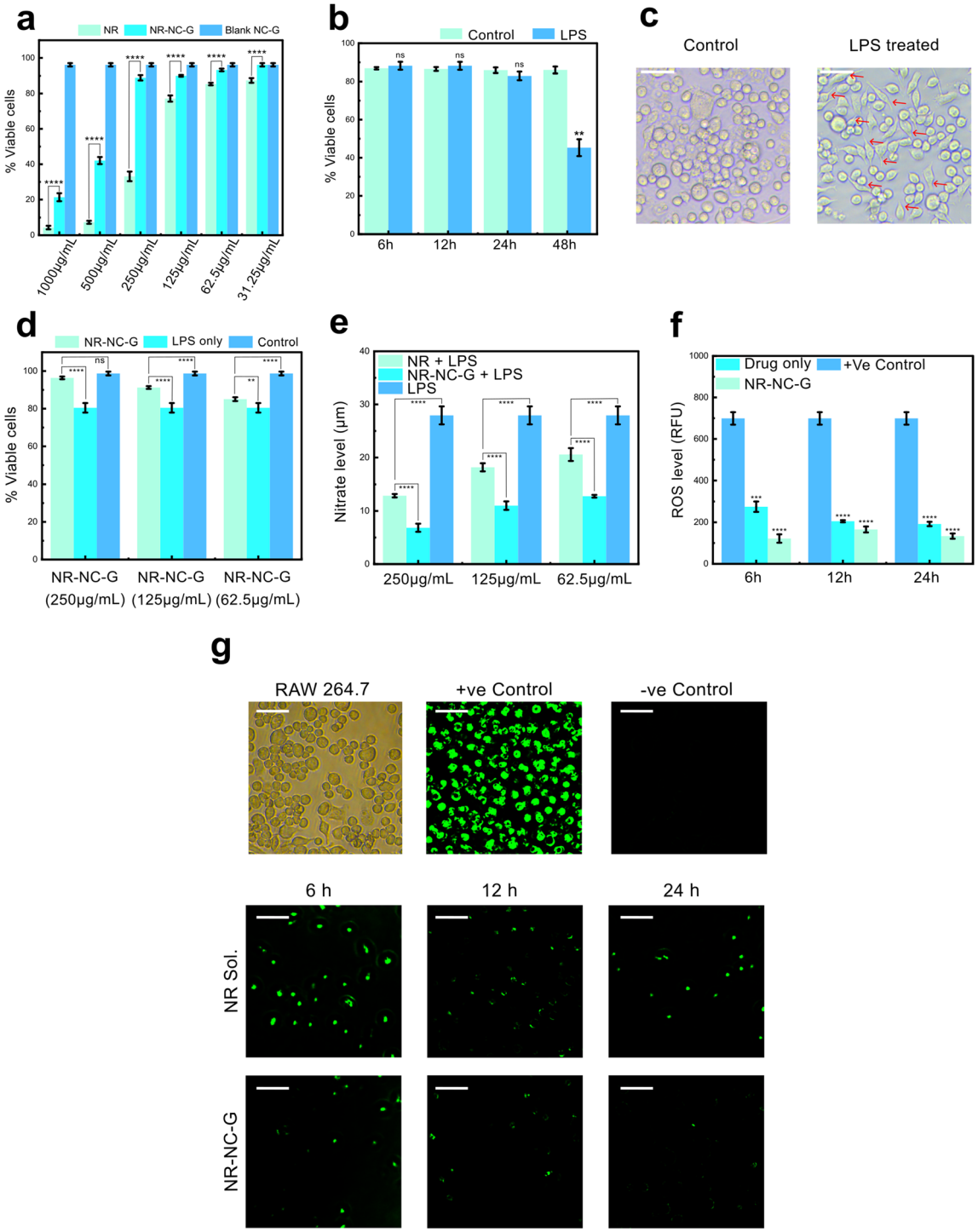

Fig. 6 *In vitro* anti-inflammatory and antioxidant evaluation in LPS-stimulated RAW 264.7 cells. (a) MTT assay comparing the cytotoxicity of NR and NR-NC-G in RAW 264.7 cells (statistical comparisons were performed using Tukey's multiple comparison test. Significance levels are indicated as follows: ****p < 0.0001, relative to the blank NC-G group); (b) MTT assay following LPS exposure at varying time intervals (statistical comparisons were performed using Sidak's multiple comparison test. Significance levels are indicated as follows: ns = 0.8548, ns = 0.7645, ns = 0.4409, **p = 0.0053, relative to the control LPS group); (c) Microscopy images illustrating morphological differences between normal and LPS-stimulated RAW 264.7 cells (scale bar = 500 μm); (d) MTT assay comparing the cytotoxicity of NR-NC-G alone and in combination with LPS (Statistical comparisons were performed using Tukey's multiple comparison test. Significance levels are indicated as follows: ns = 0.2192, ****p < 0.0001, **p = 0.0081, relative to the control group); (e) Nitrate concentration determined using the Griess reagent assay (expressed in μM) (Statistical comparisons were performed using Tukey's multiple comparison test. Significance levels are indicated as follows: ****p < 0.0001, relative to the LPS only and NR + LPS group); (f) intracellular ROS levels quantified in relative fluorescence units (RFU) (statistical comparisons were performed using Tukey's multiple comparison test. Significance levels are indicated as follows: ns = 0.8777, ns = 0.3741, *p = 0.0380, relative to the +ve control group); (g) Fluorescence imaging of intracellular ROS in RAW 264.7 cells using the DCFDA assay (scale bar = 500 μm).

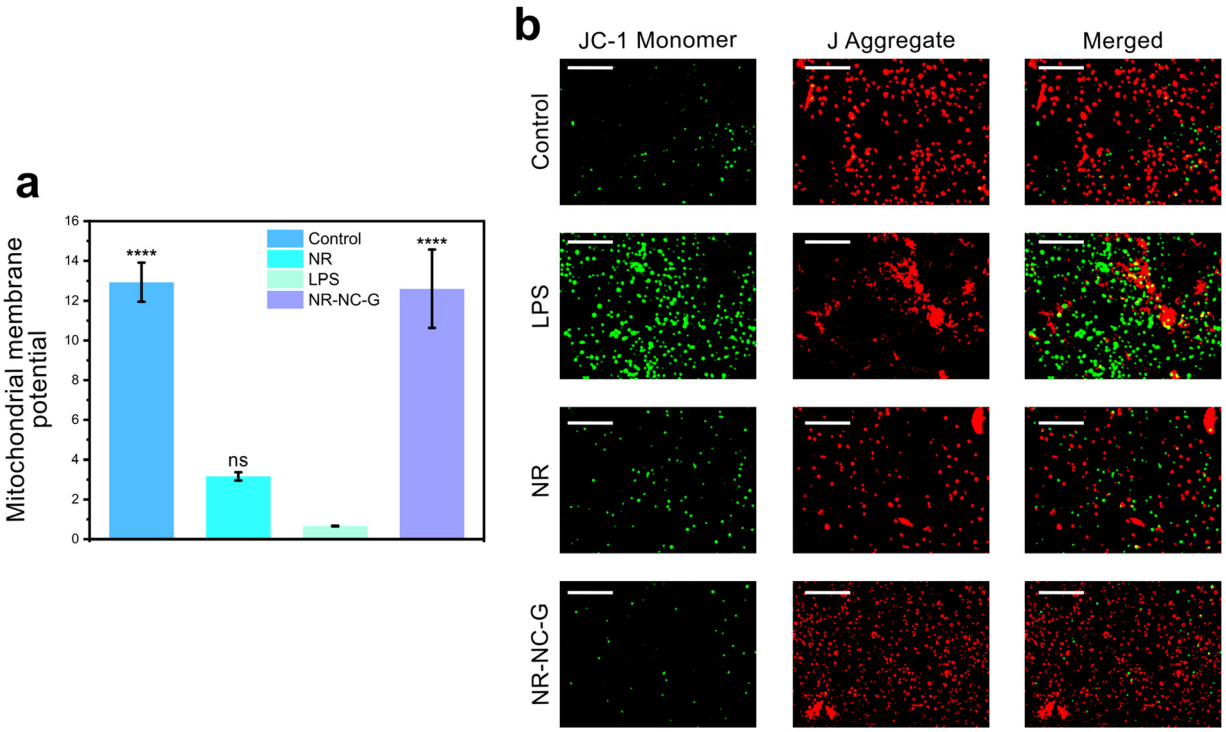

Fig. 7 (a) Evaluation of mitochondrial membrane potential following NR-NC-G treatment (statistical comparisons were performed using Dunnett's multiple comparison test. Significance levels are indicated as follows: ns = 0.0577, ****p < 0.0001, relative to the LPS only group); and (b) Fluorescence images showing changes in mitochondrial membrane potential (MMP) assessed *via* JC-1 staining (scale bar = 2 mm).

minimum doses. But at high concentrations above IC_{50}, a visible decline in cell viability was observed.

Furthermore, to examine the cytotoxic effects of LPS on RAW264.7 macrophages, cells were treated with 1 μg mL^{-1} LPS and assessed for viability at 6, 12, 24, and 48 hours (Fig. 6b). Sidak's multiple comparisons test showed no statistically significant difference in cell viability between the untreated and LPS-treated groups at 6, 12, and 24 hours ($p > 0.05$), indicating that short-term exposure to LPS does not markedly compromise macrophage viability. In contrast, by 48 hours, LPS treatment led to a pronounced decline in cell viability, compared to the control ($p = 0.0053$).

Based on these findings, concentrations of NR and NR-NC-G below 200 μg mL^{-1} were selected for subsequent experiments to ensure minimal cytotoxicity. Additionally, LPS treatment at 1 μg mL^{-1} for 6 to 24 hours was chosen as the standard condition for further assays examining inflammatory responses to obtain early immune activation.

4.5.8.1. LPS induced inflammation in cells

Morphological alterations in RAW264.7 cells upon exposure to LPS were evaluated using an inverted microscope. Cells in the untreated healthy control group showed a typical resting macrophage morphology, characterised by a round shape and smooth cellular outlines, with no visible pseudopodia (Fig. 6c – control). In contrast, cells stimulated with LPS (1 μg mL^{-1}) for 24 hours displayed morphological features indicative of macrophage activation. These included an enlargement of cell size and the extension of elongated pseudopodia, as highlighted by red arrows (Fig. 6c – LPS treated). These observations support the activation of RAW264.7 cells in response to pro-inflammatory stimulation with LPS.

4.5.8.2. Anti-inflammatory activity and NO level estimation

To evaluate the therapeutic efficacy of NR-NC-G in modulating LPS-induced cytotoxicity in RAW264.7 cells, cell viability was examined following 24-hour exposure to NR-NC-G at varying concentrations (62.5, 125, and 250 μg mL^{-1}) and compared to cells treated with LPS alone and untreated control cells. The results showed a significant restoration of cell viability in the NR-NC-G treated groups compared to the LPS-only group at all tested concentrations (Fig. 6d). At 250 μg mL^{-1}, cells treated with NR-NC-G exhibited higher cell viability compared to the LPS-only group ($p < 0.0001$). Importantly, this value was approximately similar to the untreated control group, indicating that NR-NC-G restored cellular health ($p = 0.2192$). At 125 and 62.5 μg mL^{-1}, NR-NC-G treatment also resulted in improvements in viability relative to the LPS-only group.

The nitrite levels estimation analysis revealed statistically significant differences ($p < 0.0001$) across all comparisons (Fig. 6e). At 250 μg mL^{-1}, NR-NC-G co-treated with LPS resulted in significantly lower nitrite levels compared to both

the bulk NR + LPS and LPS-only groups. Similar trends were observed at 125 μg mL^{-1}, where NR-NC-G + LPS showed a greater reduction in nitrite levels relative to the bulk NR + LPS and LPS-only groups. At 62.5 μg mL^{-1}, the nanoformulation continued to exhibit its superior effect. These results suggest that NR-NC-G exerts a significantly greater anti-inflammatory response than the bulk NR, validating the enhanced therapeutic efficacy.

4.5.8.3. Cellular ROS assessment

To evaluate intracellular ROS levels and antioxidant efficacy of the NR-NC-G formulation in LPS-stimulated RAW264.7 macrophages, DCFDA-based fluorescence imaging and quantitative fluorescence intensity measurements were performed and photographed under a fluorescent microscope. The +ve control group showed consistently high green fluorescence, confirming strong ROS generation upon inflammatory stimulation. Conversely, cells treated with the bulk NR showed time-dependent fluorescence attenuation. This trend suggests partial ROS scavenging by the bulk drug, although fluorescence remained significantly higher than that of NR-NC-G (Fig. 6f).

Cells treated with NR-NC-G showed reduced green fluorescence at all time points. At 6 hours, a faint signal was observed (RFU = 121.7), which is significantly lower than those of the bulk NR and the positive control. The fluorescence further diminished at 12 and 24 hours (RFU = 165.3 and 133.3, respectively), suggesting a sustained antioxidant effect of NR-NC-G. Tukey's multiple comparison test confirmed a significant reduction in fluorescence between the 12-hour and 24-hour timepoints in the NR-NC-G group ($p = 0.0380$), indicating that oxidative stress continued to decline over time with NR-NC-G treatment.

Microscopy images (Fig. 6g) visually validated these quantitative findings: positive control cells showed intense green fluorescence, indicative of high ROS accumulation, whereas untreated cells exhibited no fluorescence. Cells treated with bulk NR showed a modest reduction in green intensity over time. Still, cells treated with NR-NC-G showed minimal green fluorescence, specifically evident at 12 and 24 hours, highlighting the strong ROS-neutralising capacity.

4.5.8.4. Mitochondrial depolarisation

To assess mitochondrial membrane potential ($\Delta\psi_m$) in LPS-stimulated RAW264.7 macrophages, JC-1 staining was used, where healthy mitochondria are indicated by JC-1 aggregates (red fluorescence) and depolarised mitochondria by JC-1 monomers (green fluorescence). In untreated cells, high red and minimal green signals were observed, reflected by a significantly elevated red-to-green fluorescence ratio, confirming perfect mitochondrial function (Fig. 7a). On the other hand, the LPS-stimulated cells showed a drastic reduction in red fluorescence and an increased green signal (ratio ~0.66), indicating mitochondrial dysfunction.

Bulk NR-treated cells showed partial preservation of $\Delta\psi_m$, with a moderate red-to-green ratio (~3.17), compared to LPS-only cells. Importantly, this effect was significantly enhanced with NR-NC-G treatment, which restored the red-to-green fluorescence ratio to ~12.60—comparable to control levels.

Furthermore, microscopy images (Fig. 7b) supported these findings. Control cells exhibited high red fluorescence, accompanied by a low green signal, indicating intact mitochondrial function. In contrast, LPS-stimulated cells displayed strong green fluorescence and a markedly reduced red signal, indicating mitochondrial damage. Bulk NR-treated cells exhibited a transfer toward red aggregates, while still retaining residual green fluorescence. Notably, NR-NC-G-treated cells exhibited intense red fluorescence with a low green signal, and merged images indicated a restoration of mitochondrial function.

Dunnett's multiple comparisons test confirmed that the difference between LPS and the control and LPS and NR-NC-G ($p < 0.0001$) $\Delta\psi_m$ was highly significant. However, the difference between LPS and bulk NR $\Delta\psi_m$ was not statistically significant ($p = 0.0577$), suggesting that NR-NC-G gave more effective repolarisation of mitochondrial function than unentrapped NR.

5. Discussion

Plant-derived flavonoid, NR with a polyphenolic structure, has well-documented antioxidant and anti-inflammatory effects.[57] However, its therapeutic efficacy is hindered by low aqueous solubility, limited chemical stability, and permeability issues. This research aimed to overcome these problems by utilising nanocochleates (NR-NCs) embedded within a hydrogel matrix (NR-NC-G), which synergistically enhanced their bioactivity and targeted skin delivery. The data presented herein unravel not only the macroscopic and dermatokinetic advantages of NR-NC-G but also provide mechanistic insights at the molecular level.

The formulation of NR-LIPOs and their conversion into NR-NCs is done *via* a rational design under the QbD framework. The regression models, supported by high R^2 values and minimal residual error, identified Lipoid S-100 and cholesterol content as CMAs. An increase in both caused a larger PS, which may be due to the formation of multilamellar vesicles and enhanced bilayer rigidity, as cholesterol adjusts itself between phospholipid tails, decreasing fluidity. At the molecular level, cholesterol's planar steroid ring system enhances van der Waals interactions with lipid acyl chains, increasing bilayer thickness and reducing membrane permeability, thereby decreasing the %EE. The transformation into nanocochleates, confirmed *via* DLS and microscopy, is attributed to calcium-mediated inter-bilayer bridging. Calcium ions neutralise the negatively charged phospholipid, facilitating membrane stacking into cochleate cylinders. The divalent Ca^{2+} ions selectively bind to negatively charged phospholipid headgroups, leading to progressive charge neutralisation and a marked reduction in inter-bilayer repulsive forces. As this electrostatic screening increases, adjacent lamellae collapse,

fuse, and reorganise into a compacted multilamellar structure, as seen in Fig. 3f-h. Beyond a threshold Ca^{2+} concentration, this collapse is energetically sufficient to drive the characteristic folding and rolling of the stacked bilayers into the cylindrical nanocochleate architecture. Thus, the calcium level directly influences the extent and efficiency of cochleation, dictating the rigidity, completeness, and structural integrity of the resulting nanocochleates. CD spectroscopy revealed a conformational tightening of BSA, characterised by an increased β-sheet content. This structural change proves strong electrostatic and hydrophobic interactions between BSA and the NR-NC interface, helping nanocochleate stabilisation *via* surface adsorption.

DSC and XRD results showed a loss of NR crystallinity upon encapsulation, supporting molecular-level dispersion within the lipid matrix. ATR-IR peak shifts, specifically in O–H and C═O stretching regions, confirmed hydrogen bonding and hydrophobic interactions between NR and Lipoid-S-100. These forces are important in preserving the drug within the core of the bilayer. In the release study, we found that the acidic milieu of psoriatic lesions aligns closely with the accelerated NR-NC release observed at pH 5.2, enabling possible drug liberation at inflamed sites. In contrast, the markedly slower release at physiological pH 7.4 will help limit unnecessary diffusion into healthy surrounding skin. This pH-responsive behaviour supports targeted, lesion-specific delivery that can enhance therapeutic precision and overall treatment efficiency. NR-NC-G provided additional rheological stability. The gel showed pseudoplastic, shear-thinning behaviour, which is highly desirable for topical gels.

Ex vivo permeation and dermatokinetic results confirmed that NR-NC-G enhances NR deposition in skin layers. The NR-NC structure, with its strong, rolled bilayer, may facilitate transcellular penetration by disrupting tight junctions and promoting lipid fusion. The hydrogel matrix works as a holding unit or depot, maintaining a local concentration gradient that drives passive diffusion. The low K_e and higher AUC values suggest high NR accumulation in the skin, critical for managing chronic conditions like psoriasis.

NR-NC-G significantly enhanced free radical scavenging activity compared to bulk NR, with low IC_{50} values in both DPPH and H_2O_2 assays. This improvement may be due to the restricted mobility and high surface area of nanocochleates, which likely concentrate NR molecules at the interface, facilitating rapid electron donation or hydrogen atom transfer reactions. At the intracellular level in RAW 264.7, the NR-NC-G cleared ROS accumulation, as evidenced by reduced DCFDA fluorescence. This proves that NR-NC-G modulates oxidative stress by preserving the glutathione (GSH) pool and inhibiting NADPH oxidase activity. Moreover, it is possible that NR-NC-G may activate the Nrf2-Keap1 pathway, causing upregulation of antioxidant enzymes (*e.g.*, SOD, catalase), a hypothesis proved by ROS suppression over delayed time.[58]

NR-NC-G demonstrated a strong reduction of LPS-stimulated nitrite production and restored macrophage viability by inhibition of inducible nitric oxide synthase (iNOS). These effects are believed to happen through inhibition of the Toll-like receptor 4 (TLR4)/MyD88 signalling axis (Fig. 1e),[59] which is triggered by LPS and travels *via* the nuclear factor-kappa B (NF-κB) and mitogen-activated protein kinase (MAPK) pathways. At the molecular level, NR is known to inhibit IκB kinase (IKK), by preventing the degradation of IκB-α and nuclear translocation of the NF-κB p65 subunit. Additionally, NR downregulates the phosphorylation of ERK1/2, JNK, and p38 MAPK, thereby disrupting inflammatory mediators. The nano-encapsulated NR likely enhances this cycle inhibition due to sustained intracellular availability. JC-1 assays demonstrated that NR-NC-G restored $\Delta\psi_m$, a crucial factor in maintaining ATP synthesis.

This work primarily highlights the formulation perspective of the naringenin-encapsulated nano-cochleate hydrogel, emphasising its promising cellular anti-inflammatory activity and dermatokinetic behaviour, and establishes a strong foundation for topical delivery applications. While *in vivo* studies, extended safety profiling, and broader mechanistic analyses are planned as future steps, the current findings clearly demonstrate the system's potential and provide a solid platform for advancing toward more comprehensive evaluations in subsequent research.

6. Conclusion

In this study, we successfully developed a nanocochleate-based gel formulation (NR-NC-G) as an advanced and targeted topical therapy for psoriasis. A custom experimental design limited to ten trials enabled efficient optimisation by evaluating the influence of key excipients. The resulting NR-NCs demonstrated nanometric particle size, high entrapment efficiency, and sustained drug release over 36 hours when incorporated into a Carbopol gel base. *Ex vivo* dermatokinetic analysis showed enhanced NR accumulation in skin layers, supporting the formulation's skin retention capacity and potential for localised treatment. Furthermore, *in vitro* studies in LPS-stimulated RAW264.7 macrophages confirmed the anti-inflammatory and antioxidant effects of NR-NC-G, demonstrating its ability to reduce oxidative stress and highlighting its therapeutic relevance in psoriasis and paving the way for future preclinical studies.

Author contributions

ASK, ADS: conceptualisation, data curation, and writing – original draft. GK: data curation-cell line studies. KKS: writing – review & editing. RS: conceptualisation, writing – review & editing, and supervision.

Conflicts of interest

The authors declare no competing interests.

Animal ethics statement

All animal experiments were conducted in accordance with the guidelines of the Committee for the Purpose of Control and Supervision of Experiments on Animals (CPCSEA), Government of India. The experimental protocol was reviewed and approved by the Institutional Animal Ethics Committee (IAEC) of the National Institute of Pharmaceutical Education and Research (NIPER), Raebareli, under approval number NIPER/RBL/IAEC/228/SEP.2024.

Abbreviations

NR	Naringenin
NR-LIPO	Naringenin liposomes
NR-NCs	Naringenin nanocochleates
NR-NC-G	Naringenin nanochochleates hydrogel
BSA	Bovine serum albumin
ROS	Reactive oxygen species
BALB/C	Bagg albino/C
AUC	Area under curve
TNF-α	Tumour necrosis factor-α
IL-6	Interleukin-6
IL-17	Interleukin-17
NF-kB	Nuclear factor-kappa B pathway
Nrf2	Nuclear factor erythroid-derived 2
MAPK	Mitogen-activated protein kinase
HO-1	Heme oxygenase-1
PS	Hydrodynamic diameter
PDI	Polydispersity index
QBD	Quality by design
DMEM	Dulbecco's modified Eagle's medium
FBS	Fetal bovine serum
MTT	3-(4,5-Dimethylthiazol-2-yl)-2,5-diphenyltetrazolium bromide
DCFDA	Dichlorodihydrofluorescein diacetate
JC-1	5,5′,6,6′-Tetrachloro-1,1′,3,3′-tetraethylbenzimidazolocarbocyanine iodide
LPS	Lipopolysaccharide
HPLC	High-performance liquid chromatography
ICH	International Conference of Harmonization
QTPP	Quality target product profile
CQAs	Critical quality attributes
CMAs	Critical material attributes
CPPs	Critical process parameters
PS	Particle size
EE%	Encapsulation efficiency
DLS	Dynamic light scattering
CD	Circular dichroism
SEM	Scanning electron microscopy
TEM	Transmission electron microscopy
AFM	Atomic force microscopy
DSC	Differential scanning calorimetry
ATR-IR	Attenuated total reflectance – infrared spectroscopy
XRD	X-ray diffraction
RH	Relative humidity
PBS	Phosphate buffer saline
H&E	Haematoxylin and eosin
DMSO	Dimethyl sulfoxide
SFM	Serum-free medium
$\Delta\psi_m$	Mitochondrial membrane potential
ANOVA	Analysis of variance
HSD	Honest significant difference
PM	Physical mixture
AIC	Akaike information criteria
MSC	Model selection criterion
MF	Marketed formulation
LVER	Linear viscoelastic region
RFU	Relative fluorescence unit

Data availability

Data will be made available on request.

Supplementary information (SI) is available. See DOI: https://doi.org/10.1039/d5pm00268k.

Acknowledgements

The authors acknowledge the Department of Pharmaceuticals, Ministry of Chemicals and Fertilizers, Government of India, for financial support. The authors also gratefully acknowledge the CoE-NDDS and NIPER-R. The NIPER-R communication number for the research article is NIPER-R/Communication/828. The corresponding author RS acknowledges the DST-SERB for providing the SIRE fellowship with award No. SIR/2022/00678. The support provided by University of Lancashire to host the SIRE fellowship is gratefully acknowledged.

References

1 R. Keshari, A. Tharmatt, M. M. Pillai, D. Chitkara, P. Tayalia, R. Banerjee, *et al.*, Eugenol-Loaded Lipid Nanoparticles-Derived Hydrogels Ameliorate Psoriasis-like Skin Lesions by Lowering Oxidative Stress and Modulating Inflammation, *ACS Pharmacol. Transl. Sci.*, 2024, **7**, 3592–3606, DOI: 10.1021/acsptsci.4c00493.

2 O. FitzGerald, A. Ogdie, V. Chandran, L. C. Coates, A. Kavanaugh, W. Tillett, *et al.*, Psoriatic arthritis, *Nat. Rev. Dis. Primers*, 2021, **7**, 59, DOI: 10.1038/s41572-021-00293-y.

3 Q. Li, V. Chandran, L. Tsoi, D. O'Rielly, R. P. Nair, D. Gladman, *et al.*, Quantifying Differences in Heritability among Psoriatic Arthritis (PsA), Cutaneous Psoriasis (PsC) and Psoriasis vulgaris (PsV), *Sci. Rep.*, 2020, **10**, 4925, DOI: 10.1038/s41598-020-61981-5.

4 A. D. Sutar and R. Shukla, Emerging Smart Microneedle Technologies in Psoriasis: Convergence of Nanocarriers, Machine learning, and Personalized Delivery, *RSC Pharm.*, 2025, **2**(6), 1268–1291, DOI: 10.1039/D5PM00173K.

5 W. B. Kim, D. Jerome and J. Yeung, Diagnosis and management of psoriasis, *Can. Fam. Physician*, 2017, **63**, 278–285.
6 S. Makuch, M. Dróżdż, A. Makarec, P. Ziółkowski and M. Woźniak, An Update on Photodynamic Therapy of Psoriasis—Current Strategies and Nanotechnology as a Future Perspective, *Int. J. Mol. Sci.*, 2022, **23**, 9845, DOI: 10.3390/ijms23179845.
7 G. Zhang, G. Sun, H. Guan, M. Li, Y. Liu, B. Tian, *et al.*, Naringenin nanocrystals for improving anti-rheumatoid arthritis activity, *Asian J. Pharm. Sci.*, 2021, **16**, 816–825, DOI: 10.1016/j.ajps.2021.09.001.
8 R. Deenonpoe, P. Prayong, N. Thippamom, J. Meephansan and K. Na-Bangchang, Anti-inflammatory effect of naringin and sericin combination on human peripheral blood mononuclear cells (hPBMCs) from patient with psoriasis, *BMC Complementary Altern. Med.*, 2019, **19**, 168, DOI: 10.1186/s12906-019-2535-3.
9 M. Nowak-Perlak, K. Szpadel, I. Jabłońska, M. Pizon and M. Woźniak, Promising Strategies in Plant-Derived Treatments of Psoriasis-Update of In Vitro, In Vivo, and Clinical Trials Studies, *Molecules*, 2022, **27**, 591, DOI: 10.3390/molecules27030591.
10 J. A. Adetunji, K. D. Fasae, A. I. Awe, O. K. Paimo, A. M. Adegoke, J. K. Akintunde, *et al.*, The protective roles of citrus flavonoids, naringenin, and naringin on endothelial cell dysfunction in diseases, *Heliyon*, 2023, **9**, e17166, DOI: 10.1016/j.heliyon.2023.e17166.
11 D. Şahin, E.Ş Çağlar, T. Boran, A. E. Karadağ, G. Özhan and N. Üstündağ Okur, Development, characterization of naringenin-loaded promising microemulsion formulations, and demonstration of anti-aging efficacy by in vitro enzyme activity and gene expression, *J. Drug Delivery Sci. Technol.*, 2023, **84**, 104422, DOI: 10.1016/j.jddst.2023.104422.
12 D. B. Bari, S. R. Helaskar, M. B. Gagarani and C. V. Pardeshi, Nose-to-brain delivery of self-assembled curcumin-nanocochleates for glioblastoma treatment, *J. Drug Delivery Sci. Technol.*, 2025, **104**, 106557, DOI: 10.1016/j.jddst.2024.106557.
13 C. Song, R. Liu, B. Kong, Z. Gu and G. Chen, Functional hydrogels for treatment of dental caries, *Biomed. Technol.*, 2024, **5**, 73–81, DOI: 10.1016/j.bmt.2023.05.002.
14 S. Mehnath, M. Sathish Kumar, K. Chitra and M. Jeyaraj, Bone-Adhesive Hydrogel for Effective Inhibition of M. tuberculosis and Osteoblast Regeneration, *ACS Infect. Dis.*, 2023, **9**, 2269–2281, DOI: 10.1021/acsinfecdis.3c00328.
15 S. Mehnath, K. Karthikeyan and M. Jeyaraj, Mechanical Force on Hydrogel Implication on Enhanced Drug Release, Antibacterial, and M2 Macrophage Polarization: New Insights Alleviate Diabetic Wound Healing, *ACS Appl. Mater. Interfaces*, 2024, **16**(41), DOI: 10.1021/acsami.4c13633.
16 Z. Han, L. Bao, Y. Yu, Y. Zhao, M. Wang, Y. Sun, *et al.*, Injectable short-fiber hydrogel with fatigue resistance and antibacterial properties for synergistic periodontitis therapy, *Chem. Eng. J.*, 2025, **520**, 166298, DOI: 10.1016/j.cej.2025.166298.
17 K.-H. Yi, Thermal degradation of hyaluronic acid dermal fillers, *Plast. Aesthetic Res.*, 2024, **11**(56), DOI: 10.20517/2347-9264.2024.119.
18 Z. Tang, L. Deng, J. Zhang, T. Jiang, H. Xiang, Y. Chen, *et al.*, Intelligent Hydrogel-Assisted Hepatocellular Carcinoma Therapy, *Research*, 2024, **7**, 0477, DOI: 10.34133/research.0477.
19 Z. Zhang, H. Li, M. Qian, Y. Zheng, L. Bao, W. Cui, *et al.*, Up IGF-I via high-toughness adaptive hydrogels for remodeling growth plate of children, *Regener. Biomater.*, 2025, **12**, DOI: 10.1093/rb/rbaf004.
20 S. Mehnath and M. Jeyaraj, Antibiofilm and enhanced antibiotic delivery by halloysite nanotubes architected dental implant against periodontitis, *Mater. Chem. Phys.*, 2023, **295**, 127061, DOI: 10.1016/j.matchemphys.2022.127061.
21 M. Arjama, S. Mehnath, M. Rajan and M. Jeyaraj, Engineered Hyaluronic Acid-Based Smart Nanoconjugates for Enhanced Intracellular Drug Delivery, *J. Pharm. Sci.*, 2023, **112**, 1603–1614, DOI: 10.1016/j.xphs.2021.10.005.
22 D. K. Jha, D. S. Shah, S. R. Talele and P. D. Amin, Correlation of two validated methods for the quantification of naringenin in its solid dispersion: HPLC and UV spectrophotometric methods, *SN Appl. Sci.*, 2020, **2**, 698, DOI: 10.1007/s42452-020-2536-3.
23 R. Bhandari, A. Kuhad, J. K. Paliwal and A. Kuhad, Development of a new, sensitive, and robust analytical and bio-analytical RP-HPLC method for *in vitro* and *in vivo* quantification of naringenin in polymeric nanocarriers, *J. Anal. Sci. Technol.*, 2019, **10**, 11, DOI: 10.1186/s40543-019-0169-1.
24 A. D. Sutar, R. K. Verma and R. Shukla, Quality by Design in Pulmonary Drug Delivery: A Review on Dry Powder Inhaler Development, Nanotherapy Approaches, and Regulatory Considerations, *AAPS PharmSciTech*, 2024, **25**, 178, DOI: 10.1208/s12249-024-02900-z.
25 S. J. Nadaf and S. G. Killedar, Curcumin nanocochleates: Use of design of experiments, solid state characterization, in vitro apoptosis and cytotoxicity against breast cancer MCF-7 cells, *J. Drug Delivery Sci. Technol.*, 2018, **47**, 337–350, DOI: 10.1016/j.jddst.2018.06.026.
26 S. Hatem and M. El-Kayal, Novel anti-psoriatic nanostructured lipid carriers for the cutaneous delivery of luteolin: A comprehensive *in vitro* and *in vivo* evaluation, *Eur. J. Pharm. Sci.*, 2023, **191**, 106612, DOI: 10.1016/j.ejps.2023.106612.
27 M. Tilawat and S. Bonde, Curcumin and quercetin loaded nanocochleates gel formulation for localized application in breast cancer therapy, *Heliyon*, 2023, **9**, e22892, DOI: 10.1016/j.heliyon.2023.e22892.
28 T. Shanmugam, N. Joshi, N. Ahamad, A. Deshmukh and R. Banerjee, Enhanced absorption, and efficacy of oral self-assembled paclitaxel nanocochleates in multi-drug resistant colon cancer, *Int. J. Pharm.*, 2020, **586**, 119482, DOI: 10.1016/j.ijpharm.2020.119482.
29 D. (Chau Thuy) Nguyen, J. Dowling, R. Ryan, P. McLoughlin and L. Fitzhenry, Controlled release of nar-

ingenin from soft hydrogel contact lens: An investigation into lens critical properties and in vitro release, *Int. J. Pharm.*, 2022, **621**, 121793, DOI: 10.1016/j.ijpharm.2022.121793.

30 M. G. El-Melegy, H. M. Eltaher, A. Gaballah and A. H. El-Kamel, Enhanced oral permeability of Trans-Resveratrol using nanocochleates for boosting anticancer efficacy; *in vitro* and *ex vivo* appraisal, *Eur. J. Pharm. Biopharm.*, 2021, **168**, 166–183, DOI: 10.1016/j.ejpb.2021.08.020.

31 Y. Tomar, S. Maheshwari, S. Gorantla and G. Singhvi, Curcumin loaded liquid crystalline nanoparticles for enhanced topical application: Design, characterization, ex vivo and dermatokinetic evaluation, *J. Drug Delivery Sci. Technol.*, 2024, **92**, 105391, DOI: 10.1016/j.jddst.2024.105391.

32 X. Yang, Y. Tang, M. Wang, Y. Wang, W. Wang, M. Pang, *et al.*, Co-delivery of methotrexate and nicotinamide by cerosomes for topical psoriasis treatment with enhanced efficacy, *Int. J. Pharm.*, 2021, **605**, 120826, DOI: 10.1016/j.ijpharm.2021.120826.

33 A. G. Yurtsever, A. Ekmekcioglu, M. Muftuoglu, S. Güngör and M. S. Erdal, Formulation development and evaluation of fluvastatin loaded transethosomes: Characterization, stability, in vitro dermal penetration, cytotoxicity and anti-psoriatic activity studies, *J. Drug Delivery Sci. Technol.*, 2024, **91**, 105234, DOI: 10.1016/j.jddst.2023.105234.

34 L. L. David, A. Daniels, S. Habib and M. Singh, Gold nanoparticles in transferrin-targeted dual-drug delivery in vitro, *J. Drug Delivery Sci. Technol.*, 2023, **90**, 105168, DOI: 10.1016/j.jddst.2023.105168.

35 F. R. Wibowo, O. A. Saputra, W. W. Lestari, M. Koketsu, R. R. Mukti and R. Martien, pH-Triggered Drug Release Controlled by Poly(Styrene Sulfonate) Growth Hollow Mesoporous Silica Nanoparticles, *ACS Omega*, 2020, **5**, 4261–4269, DOI: 10.1021/acsomega.9b04167.

36 A. Bergal, M. Andac and F. Trotta, Cyclodextrin-based chemically modified pH-Responsive new kind of aldehyde-functionalized nanosponge nanoparticles for doxorubicin hydrochloride delivery, *J. Drug Delivery Sci. Technol.*, 2025, **107**, 106853, DOI: 10.1016/j.jddst.2025.106853.

37 Y. Zhang, M. Huo, J. Zhou, A. Zou, W. Li, C. Yao, *et al.*, DDSolver: an add-in program for modeling and comparison of drug dissolution profiles, *AAPS J.*, 2010, **12**, 263–271, DOI: 10.1208/s12248-010-9185-1.

38 A. Kumar, B. Valamla, P. Thakor, P. S. Chary, N. Rajana and N. K. Mehra, Development and evaluation of nanocrystals loaded hydrogel for topical application, *J. Drug Delivery Sci. Technol.*, 2022, **74**, 103503, DOI: 10.1016/j.jddst.2022.103503.

39 M. Behera, P. Mahale, A. Gowtham, A. D. Sutar, R. K. Kaundal and R. Shukla, Quality by design based hydrogel formulation of 4-Octyl itaconate-loaded nanostructured lipid carriers for epidermal restoration in atopic dermatitis, *J. Pharm. Invest.*, 2025, 1–22, DOI: 10.1007/s40005-025-00748-4.

40 V. Kokol, Y. B. Pottathara, M. Mihelčič and L. S. Perše, Rheological properties of gelatine hydrogels affected by flow- and horizontally-induced cooling rates during 3D cryo-printing, *Colloids Surf., A*, 2021, **616**, 126356, DOI: 10.1016/j.colsurfa.2021.126356.

41 D. Mathure, A. D. Sutar, H. Ranpise, A. Pawar and R. Awasthi, Preparation and Optimization of Liposome Containing Thermosensitive In Situ Nasal Hydrogel System for Brain Delivery of Sumatriptan Succinate, *Assay Drug Dev. Technol.*, 2023, **21**, 3–16, DOI: 10.1089/adt.2022.088.

42 L. Angeli, K. Morozova and M. Scampicchio, A kinetic-based stopped-flow DPPH· method, *Sci. Rep.*, 2023, **13**, 7621, DOI: 10.1038/s41598-023-34382-7.

43 R. T. Polez, M. A. Ajiboye, M. Österberg and M. M. Horn, Chitosan hydrogels enriched with bioactive phloroglucinol for controlled drug diffusion and potential wound healing, *Int. J. Biol. Macromol.*, 2024, **265**, 130808, DOI: 10.1016/j.ijbiomac.2024.130808.

44 F. S. Alfehaid, A. B. Nair, H. Shah, B. Aldhubiab, J. Shah, V. Mewada, *et al.*, Enhanced transdermal delivery of apremilast loaded ethosomes: Optimization, characterization and in vivo evaluation, *J. Drug Delivery Sci. Technol.*, 2024, **91**, 105211, DOI: 10.1016/j.jddst.2023.105211.

45 K. Van Bocxlaer, E. Gaukel, D. Hauser, S. H. Park, S. Schock, V. Yardley, *et al.*, Topical Treatment for Cutaneous Leishmaniasis: Dermato-Pharmacokinetic Lead Optimization of Benzoxaboroles, *Antimicrob. Agents Chemother.*, 2018, **62**, DOI: 10.1128/AAC.02419-17.

46 A. Sharma, D. K. Upadhyay, G. S. Sarma, N. Kaur, G. D. Gupta, R. K. Narang, *et al.*, Squalene integrated NLC based gel of tamoxifen citrate for efficient treatment of psoriasis: A preclinical investigation, *J. Drug Delivery Sci. Technol.*, 2020, **56**, 101568, DOI: 10.1016/j.jddst.2020.101568.

47 K. Saini, N. Modgill, K. Singh and V. Kakkar, Tetrahydrocurcumin Lipid Nanoparticle Based Gel Promotes Penetration into Deeper Skin Layers and Alleviates Atopic Dermatitis in 2,4-Dinitrochlorobenzene (DNCB) Mouse Model, *Nanomaterials*, 2022, **12**, 636, DOI: 10.3390/nano12040636.

48 A. Qadir, M. Aqil, A. Ali, M. H. Warsi, M. Mujeeb, F. J. Ahmad, *et al.*, Nanostructured lipidic carriers for dual drug delivery in the management of psoriasis: Systematic optimization, dermatokinetic and preclinical evaluation, *J. Drug Delivery Sci. Technol.*, 2020, **57**, 101775, DOI: 10.1016/j.jddst.2020.101775.

49 S. S. Alqarni, M. Afzal, F. A. Al-Abbasi, E. Moglad, A. S. Bawadood, N. A. R. Almalki, *et al.*, Exploring acemannan-loaded nanogel formulation for the treatment of IMQ-induced psoriasis-like inflammation: In vitro characterization and in vivo efficacy assessment, *Int. Immunopharmacol.*, 2025, **148**, 114064, DOI: 10.1016/j.intimp.2025.114064.

50 J. Wu, S. Liu, H. Zhang, X. Zhang, J. Xue, Z. Li, *et al.*, Amlexanox ameliorates imiquimod-induced psoriasis-like dermatitis by inhibiting Th17 cells and the NF-κB signal

pathway, *Biomed. Pharmacother.*, 2025, **184**, 117922, DOI: 10.1016/j.biopha.2025.117922.

51 V. K. Singh, D. Sahoo, K. Agrahari, A. Khan, P. Mukhopadhyay, D. Chanda, *et al.*, Anti-inflammatory, anti-proliferative and anti-psoriatic potential of apigenin in RAW 264.7 cells, HaCaT cells and psoriasis like dermatitis in BALB/c mice, *Life Sci.*, 2023, **328**, 121909, DOI: 10.1016/j.lfs.2023.121909.

52 S. Thakur, M. M. Anjum, S. Jaiswal, A. K. Gautam and P. S. Rajinikanth, Tazarotene-calcipotriol loaded Nanostructured lipid carrier enriched hydrogel: A novel dual drug synergistic approach towards Psoriasis management, *J. Drug Delivery Sci. Technol.*, 2023, **88**, 104944, DOI: 10.1016/j.jddst.2023.104944.

53 Y. Tian, S. Zhou, R. Takeda, K. Okazaki, M. Sekita and K. Sakamoto, Anti-inflammatory activities of amber extract in lipopolysaccharide-induced RAW 264.7 macrophages, *Biomed. Pharmacother.*, 2021, **141**, 111854, DOI: 10.1016/j.biopha.2021.111854.

54 A. Shariev, S. Menounos, A. J. Laos, P. Laxman, D. Lai, S. Hua, *et al.*, Skin protective and regenerative effects of RM191A, a novel superoxide dismutase mimetic, *Redox Biol.*, 2021, **38**, 101790, DOI: 10.1016/j.redox.2020.101790.

55 C. Jiang, J. Zhang, H. Xie, H. Guan, R. Li, C. Chen, *et al.*, Baicalein suppresses lipopolysaccharide-induced acute lung injury by regulating Drp1-dependent mitochondrial fission of macrophages, *Biomed. Pharmacother.*, 2022, **145**, 112408, DOI: 10.1016/j.biopha.2021.112408.

56 D. Ji, J. Yin, D. Li, C. Zhu, J. Ye and Y. Pan, Effects of inflammatory and anti-inflammatory environments on the macrophage mitochondrial function, *Sci. Rep.*, 2020, **10**, 20324, DOI: 10.1038/s41598-020-77370-x.

57 R. Joshi, Y. A. Kulkarni and S. Wairkar, Pharmacokinetic, pharmacodynamic and formulations aspects of Naringenin: An update, *Life Sci.*, 2018, **215**, 43–56, DOI: 10.1016/j.lfs.2018.10.066.

58 J. Xu, H. Chen, H. Qian, F. Wang and Y. Xu, Advances in the modulation of ROS and transdermal administration for anti-psoriatic nanotherapies, *J. Nanobiotechnol.*, 2022, **20**, 448, DOI: 10.1186/s12951-022-01651-y.

59 S. Han, H. Gao, S. Chen, Q. Wang, X. Li, L.-J. Du, *et al.*, Procyanidin A1 Alleviates Inflammatory Response induced by LPS through NF-κB, MAPK, and Nrf2/HO-1 Pathways in RAW264.7 cells, *Sci. Rep.*, 2019, **9**, 15087, DOI: 10.1038/s41598-019-51614-x.